



Università degli Studi Mediterranea di Reggio Calabria
Archivio Istituzionale dei prodotti della ricerca

A methodology based on GEOBIA and WorldView-3 imagery to derive vegetation indices at tree crown detail in olive orchards

This is the peer reviewed version of the following article:

Original

A methodology based on GEOBIA and WorldView-3 imagery to derive vegetation indices at tree crown detail in olive orchards / Solano, F; Di Fazio, S; Modica, G. - In: INTERNATIONAL JOURNAL OF APPLIED EARTH OBSERVATION AND GEOINFORMATION. - ISSN 1569-8432. - 83:(2019). [10.1016/j.jag.2019.101912]

Availability:

This version is available at: <https://hdl.handle.net/20.500.12318/830> since: 2020-11-23T22:38:41Z

Published

DOI: <http://doi.org/10.1016/j.jag.2019.101912>

The final published version is available online at: <https://www.sciencedirect.com>.

Terms of use:

The terms and conditions for the reuse of this version of the manuscript are specified in the publishing policy. For all terms of use and more information see the publisher's website

Publisher copyright

This item was downloaded from IRIS Università Mediterranea di Reggio Calabria (<https://iris.unirc.it/>) When citing, please refer to the published version.

(Article begins on next page)

This is the peer reviewed version of the following article
Francesco Solano, Salvatore Di Fazio, Giuseppe Modica,
A methodology based on GEOBIA and WorldView-3 imagery to derive vegetation indices
at tree crown detail in olive orchards, International Journal of Applied Earth Observation
and Geoinformation, Volume 83, 2019, 101912,ISSN 0303-2434,
which has been published in final doi <https://doi.org/10.1016/j.jag.2019.101912>.
(<https://www.sciencedirect.com/science/article/pii/S0303243418312017>)
The terms and conditions for the reuse of this version of the manuscript are specified in
the publishing policy. For all terms of use and more information see the publisher's
website.

3
4 **A methodology based on GEOBIA and WorldView-3 imagery to derive**
5 **vegetation indices at tree crown detail in olive orchards**

6 Francesco Solano , Salvatore Di Fazio, Giuseppe Modica

7 University of Reggio Calabria, Loc. Feo di Vito, 89129, Reggio Calabria, Italy

8
9
10 Received 13 December 2018, Revised 20 June 2019, Accepted 28 June 2019, Available online 5 July 2019.

11
12
13
14 Solano, F., Di Fazio, S., & Modica, G. (2019). A methodology based on GEOBIA and
15 WorldView-3 imagery to derive vegetation indices at tree crown detail in olive orchards.
16 *International Journal of Applied Earth Observation and Geoinformation*, 83(November
17 2019), 101912. <https://doi.org/10.1016/j.jag.2019.101912>

A methodology based on GEOBIA and WorldView-3 imagery to derive Vegetation Indices at tree crown detail in olive orchards

Abstract

Precision agriculture (PA) is becoming an essential practice for the implementation of sustainable agriculture that encompasses the efficient use of resources and a systematic crops monitoring. The increasing temporal and spatial resolution of satellite imagery, coupled with their availability and decreasing costs, create new possibilities for generating accurate datasets on different crops variables, more frequently available as ready-to-use data. The availability of very high-resolution (VHR) satellite imagery, such as the WorldView-3 (WV-3), leads to the advanced potential of satellite Remote Sensing (RS), becoming in the last decade one of the main data source in precision agriculture (PA). In the broad overview of these procedures, geographic object-based image classification (GEOBIA) techniques, gained broad interest as methods to produce geographic information in GIS-ready format. In this paper, methodologies for a semiautomatic process workflow is presented, providing olive tree crown detection in two different olive orchards in Calabria (Italy), collected by means of GEOBIA procedures, in order to investigate olive tree spectral behavior and the reliability of WV-3 derived vegetation indices (VIs). The semi-automated classification method, accomplished by imagery pre-processing steps, may constitute an operational processing chain for mapping and monitoring olive orchards at tree scale detail. Five VIs were investigated: Normalized Difference Vegetation Index (NDVI), Modified Soil Adjusted Vegetation Index 2 (MSAVI 2), Normalized Difference Red Edge Vegetation Index (NDRE), Modified Chlorophyll Absorption Ratio Index Improved (MCARI2), and NDVI2. The obtained results were statistically tested and their accuracy assessed. Thematic accuracy ranges from 95.33% to 96% in both study areas with an overall tree detection rate of 96.8%. Statistical analysis showed that the major differences in spectral behavior, over different plots of the investigated olive orchards, are mainly due to the component of the red-infrared regions of the electromagnetic spectrum (EM), where the red-edge becomes important in assessing the state of general vigor. Moreover, the proposed methodology increases the possibility of detecting tree stress at earlier stages and the benefits of using satellite-based approaches in terms of: larger area coverage, less processing and operator interaction coupled with more spectral information, thus reducing the need to collect costly reference data sampling.

Keywords: Olive trees' crown extraction, Vegetation Indices (VIs); Worldview-3 (WV-3); geographic object-based image classification (GEOBIA); spectral behavior; Precision Agriculture (PA), Olive orchards; Satellite Remote Sensing

58 **1. Introduction**

59 Olive (*Olea europaea* L.) is one of most ancient plants cultivated by human communities. Its
60 domestication dates back prior 6000 BC (in the areas of present Syria and Turkey) while the earliest
61 archaeological testimonies related to olive-oil production (presses and mortars found in Israel) date to
62 around 4500 BC. In the Mediterranean area, the cultivation of olive acquired great importance when it
63 reached the mainland and the islands of Greece, particularly Crete. Here, it soon became an important
64 driver of development for the Minoan civilization that dominated the Mediterranean basin from
65 around 2700 to 1500 BC. When the Greek civilization expanded throughout the Mediterranean basin,
66 the cultivation of olive and the production of olive oil became an important economic activity also in
67 the new colonies of Magna Graecia, established in southern Italy from the VIII century BC, and in the
68 following Roman civilization. Olive oil, extracted in an ever more efficient way thanks to innovation
69 in dedicated technology, had many and varied uses: culinary, as fuel for lamps, for lubrication, food
70 preservation, cosmetics, ritual anointing. Olive-oil this way became, and still is, a recurring element in
71 all the cultural expressions of the Mediterranean peoples (Foxhall, 2007; Tardi, 2014), as well as one
72 of the main sources of income and employment (de Graaff and Eppink, 1999). Currently, olive groves
73 are widespread in the Mediterranean Basin (Loumou and Giourga, 2003) and represent a recognized
74 sign of several Mediterranean historical rural landscapes, also marking significantly their character (Di
75 Fazio and Modica, 2018). Moreover, in the Mediterranean basin, falls the great majority of 9.4 million
76 ha of olive groves cultivated globally (Vossen, 2007).

77 Presently, the Mediterranean area is the most important olive and olive oil world-producing region.
78 With reference to average values of the last five years, world olive oil yearly production is about 3
79 million tons, 93% of which comes from the Mediterranean area (International Olive Council, 2018).
80 An important role is played by four European Mediterranean countries, Spain, Italy, Greece and
81 Portugal. Spain progressively increased its production since the late 1980s (Buckland and Gonzales,
82 2010), thanks to innovation, modernization and intensification of oliviculture, now being the world
83 leader with 1.3 million tons olive oil produced, equal to 43% of world production, followed by Italy

84 (0.35 million tons, ~12% world production). Most of Italian production comes from Apulia and
85 Calabria, 48% and 17% respectively (ISMEA, 2018).

86 With reference to the period 2013-18, while the average yearly production of Spain largely exceeds
87 the national consumption, the quantity of olive oil produced in Italy is about 60% the oil consumed,
88 that is not enough to reach self-sufficiency. In Italy, therefore it is apparent the need to increase the
89 national olive oil production as well as to improve its quality; this, to fully match internal consumer's
90 demand, and better compete with other Mediterranean countries in export towards countries such as
91 USA and Japan where the Mediterranean diet and high quality extra-virgin olive oil are having a
92 growing popularity. In the framework of a continuously evolving global market, olive and olive oil
93 industries should introduce new and innovative technologies in order to enhance their productivity and
94 improve their competitiveness (Benalia et al., 2017). Precision agriculture (PA) methodologies and
95 technologies can be currently considered as the most reliable and cost effective approach for achieving
96 both sustainable environmental management and efficient crop production, thus revealing themselves
97 as an important tool to support decision-making and improve the competitiveness of agriculture. The
98 recent and fast development in sensory technologies and the parallel progressive reduction of their
99 costs, have allowed ever more users to benefit from applications of PA. Agriculture represents an
100 important economic sector for the application of geographic information systems (GIS) and remote
101 sensing (RS) data and methods. Providing spatial segmentation and within-field variability
102 information, RS is one of the most powerful tool to monitor and manage field crops in the framework
103 of PA techniques (Sepulcre-Cantò et al., 2005). PA also benefits from RS derived information on plant
104 photosynthetic processes at various spatial and temporal scales (Kumar and Monteith, 1981; Prince,
105 1990; Veroustraeate et al., 2002). Plants' biophysical characteristics can be spectrally characterized by
106 vegetation indices (VIs) which can be defined as radiometric measurements without unit. They are
107 calculated as ratios or differences of two or more bands in the visible (VIS), near infra-red (NIR) and
108 short wave IR (SWIR) portion of the EM spectrum remotely detected by satellite, aerial and terrestrial
109 platforms. VIs are primarily intended for use in PA (Roberts et al., 2011) and most of them measure
110 the reflectance of red, NIR and the red-edge (RE) portion of the EM spectrum in the reflectance curve
111 that describes the transition from absorption by chlorophyll to dispersion. The use of NIR

112 measurements, characterized by a greater penetration through the canopy cover, allows for estimating
113 the total amount of green material (Modica et al., 2019). Measurement in the RE region allow these
114 indices to be more sensitive to minor changes in vegetation health, particularly in dense vegetation
115 conditions (Pauly, 2014).

116 The usefulness of a VI is determined by its high correlation with plants biophysical parameters and the
117 low sensitivity to the factors that hinder the interpretation of RS data, such as soil background, terrain
118 roughness, non-photosynthetic plant elements, atmosphere, viewing and illumination geometry
119 (Wojtowicz et al., 2016). The increasing geometric and temporal resolution and the positional
120 accuracy of satellite sensors in the last fifteen years, however, allow the assessment of problems such
121 as vegetation health, drought stress, fruit yield assessment and flooding (Bausch and Khosla, 2010;
122 Calderón et al., 2015, 2013; Calvão and Palmeirim, 2004; Hunt et al., 2013; Villalobos et al., 2006;
123 Wallace et al., 2004). The primary platforms used to obtain RS imagery were satellites and piloted
124 aircrafts, but they frequently did not deliver adequate spatial and temporal resolutions (Nebikera et al.,
125 2008). The advent of very high-resolution (VHR) imagery such as those provided by WorldView-3
126 (WV-3) (DigitalGlobe Inc., www.digitalglobe.com), has led to the advanced potential of satellite RS,
127 which in the near future will probably become the main methodology of data acquisition from
128 agricultural field parcels. In addition to the development of vehicles and sensors for the acquisition of
129 VHR imagery, even multispectral imaging technologies have been implemented to provide
130 increasingly efficient and reliable information extraction methods. In the broad overview of these
131 procedures, geographic object-based image classification (GEOBIA) techniques, gained broad interest
132 as methods to produce geographic information in GIS-ready format (Blaschke et al., 2014). This
133 approach considers not only the identification of the ground coverage at the pixel level, but also the
134 organization of these pixels in groups (segments) that correspond to objects in the real world
135 (Blaschke, 2010; Chepkochei, 2011). The analysis of scientific literature shows that several researches
136 deal with the use of WV imagery coupled with GEOBIA techniques. Different research topics ranging
137 from tree species classification to greenhouse detection were investigated (Aguilar et al., 2013; Alrassi
138 et al., 2016; Chepkochei, 2011; Chuang and Shiu, 2016; Gaertner, 2017; Majid et al., 2016; Mutanga
139 et al., 2015; Shahi et al., 2017; Shojanoori et al., 2016; Waser et al., 2014). On the other hand,

140 literature reports very few experiences dealing with the application of WV-3 in studying the
141 physiological status of individual tree (Anderson et al., 2018; Koenig and Gueguen, 2016;
142 Palchowdhuri et al., 2018; Rahman et al., 2018; Robson et al., 2017). This is mainly due to the very
143 recent availability of WV-3 imagery (August 2014) and to the high cost required to access these data
144 (Zartaloudis et al., 2015).

145 Taking into consideration the aforementioned research findings, the present paper has three main
146 research goals: a) to provide a semiautomatic workflow aimed at the olive tree crown detection and
147 extraction by means of GEOBIA techniques; b) to investigate the reliability of WV-3 derived VIs in
148 analyzing olive trees' vegetative vigor without ground radiometric measures; c) to provide a quick and
149 cost saving procedure not needing expensive ground truths collection in the framework of PA
150 techniques.

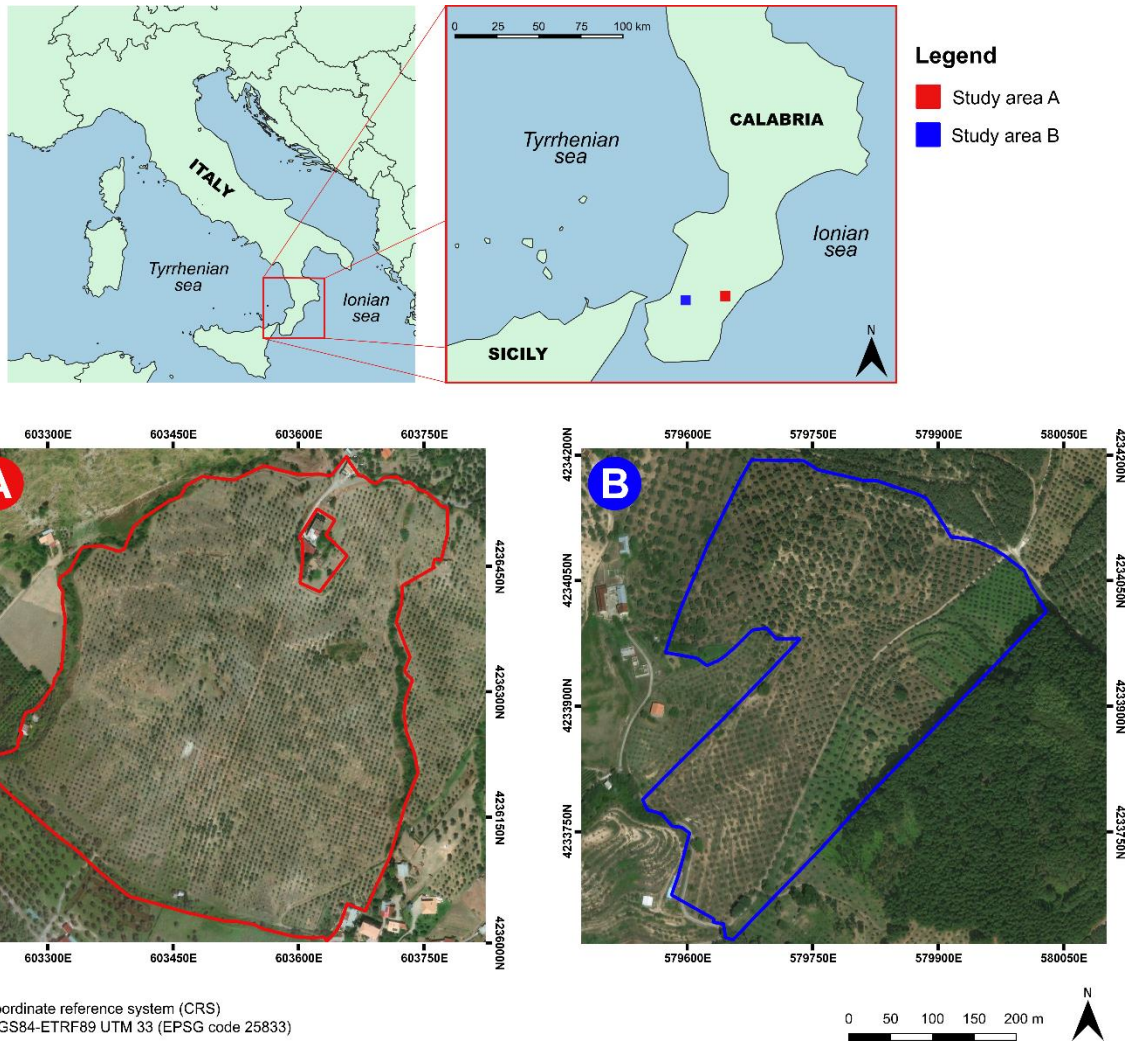
151 The structure of the present paper is as follows. In section 2, the study areas are presented and
152 described, while section 3 deals with materials and methods, providing details on data processing
153 workflow, pre-processing steps (subsections 3.1-3.2), the analyzed VIs, and GEOBIA procedures
154 aimed at the tree crown extraction (subsections 3.3.-3.6). Section 4 is devoted to show the obtained
155 results, discussed in section 5 and, and finally, section 6, deals with conclusions and final remarks.

156

157 **2. Study areas**

158 The study was carried out in Calabria, a region characterized by high hydrogeological risk (Petrucci et
159 al., 2009), and in which olive groves assume a significant role in reducing rainfall's losses. These
160 systems include agro-forestry stands, traditional groves and new intensive orchards, with a high yield
161 variability due to the co-existence of extensive orchards with few trees per hectare and intensive ones
162 having more than 600 trees ha⁻¹ (Bernardi et al., 2016). In the region, which is located in the very
163 South of the Italian peninsula, the province of Reggio Calabria is the most representative. There, two
164 specialized olive orchards identified as A and B and managed according to organic farming methods
165 were selected to develop and evaluate our proposed method (Fig. 1). Both study areas were chosen in

166 relation to their extension and cultivation characteristics, they do not differ in crop management
 167 system, while differ in tree shapes and dimensions, as well as according to the plantation age.
 168



169  Coordinate reference system (CRS)
 170 WGS84-ETRF89 UTM 33 (EPSG code 25833)
 171 **Fig. 1.** Study areas localization based on high spatial resolution WorldView-3 satellite images presented in true color band
 172 combination (RGB 5-3-2) (Acquisition date: A, 24 June 2016; B, 2 July 2016).

173 The orchards chosen are characterized as follows. Olive orchard A is located in in the municipality of
 174 Gerace covering a surface of 21.42 ha. Cultivar is “Grossa di Gerace” and olive trees’ age is about 20
 175 years while a traditional single-tree 6m x 6m planting distance is adopted. Soil is mostly clay,
 176 naturally grassy and periodically mowed in spring season, while irrigation is not adopted neither in
 177 drought periods. The only treatments provided are based on copper during dormancy.
 178 Olive orchard B is located in the municipality of Delianuova (Fig. 1) covering a surface of 14.28 ha.
 179 Olive trees’ age is about 15 years and mixed cultivars “Ottobratica” (80%) and “Leccino” (20%) are

180 produced adopting a traditional single-tree 6m x 6m planting distance. Soil is mostly with medium
181 texture, naturally grassy and periodically mowed in spring, summer and autumn seasons, while
182 irrigation is not adopted even in drought periods. Also in this case, only copper treatments during
183 dormancy are provided.

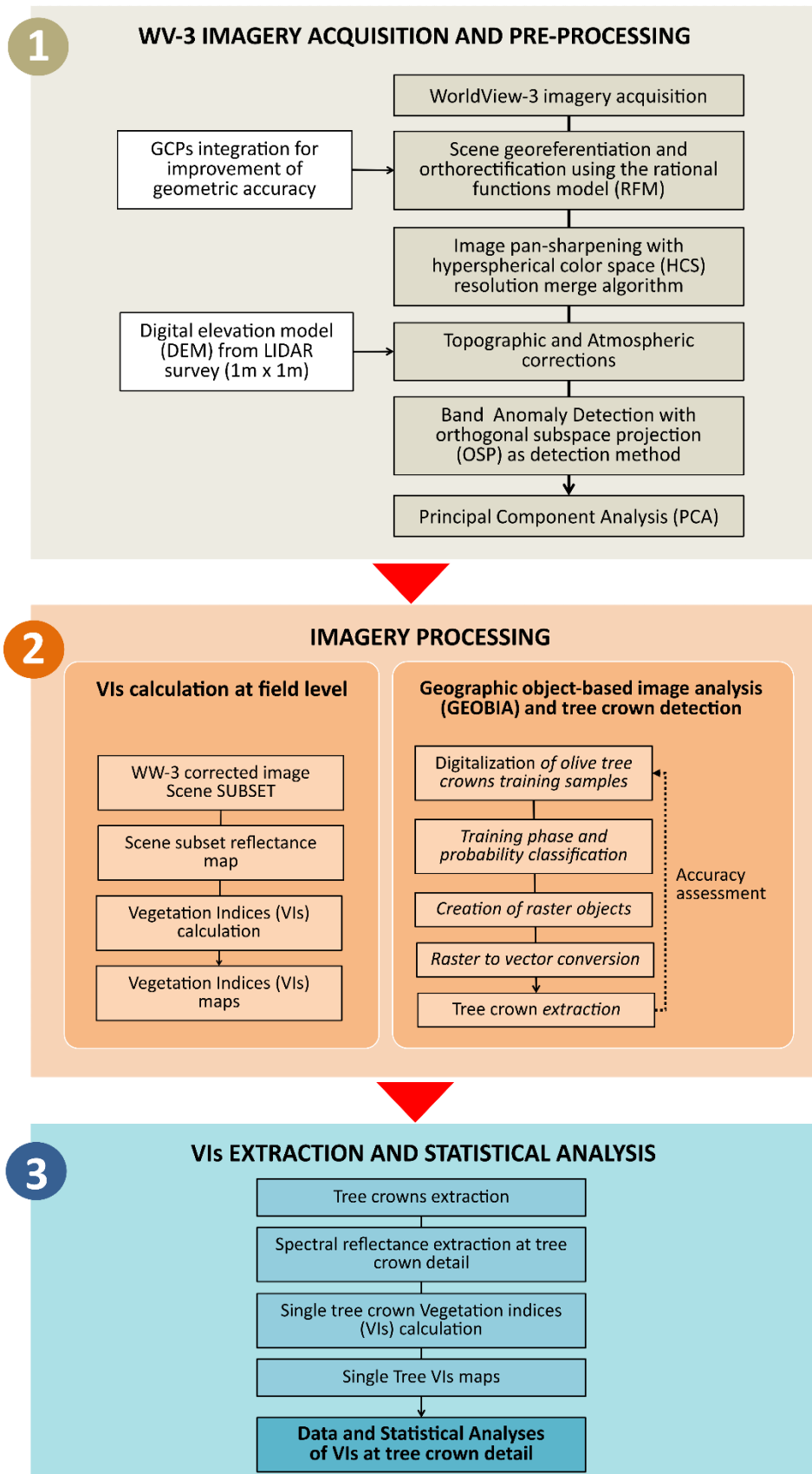
184 Within each study area, 4 plots of 2150 m² (8 in total), respectively labelled as A₁, A₂, A₃, A₄ and B₁,
185 B₂, B₃, B₄, and with different potential productivity, were identified in order to deepen investigation
186 and compare spectral behavior at tree crown detail.

187

188 **3. Material and Methods**

189 **3.1 Data processing workflow**

190 Having preliminarily defined a specific workflow in the spatial modeler environment in Erdas
191 Imagine® 2018 software (Fig. 2), we implemented a semi-automated geoprocessing operations based
192 on customized RS imagery processing procedures. The full procedure can be singled out in three main
193 phases: 1) WV-3 imagery acquisition and pre-processing analysis; 2) imagery processing through
194 GEOBIA followed by tree crown detection and extraction, and generation of VIs maps; 3) VIs
195 extraction at tree crown detail and statistical analyses for the reliability assessment of the obtained
196 results.



197

198

199

200

Fig. 2. A synthetic flow-chart showing the implemented semi-automated processing workflow to derive vegetation indices (VIs) at tree crown details from WorldView-3 (WW3) imagery.

201 **3.2 Satellite Data Acquisition and pre-processing steps**

202 A pair of WV-3 satellite images were acquired on 24 June 2016 for study area A and on 2 July 2016
203 for B and processed. WV-3 dataset consisted of eight multispectral bands and one panchromatic band
204 images at 16 bit of radiometric resolution (Table 1). Both images were first georeferenced according to
205 the coordinate reference system (CRS) WGS84-ETRF89 UTM 33 (EPSG code 25833) then
206 orthorectified using the rational function model (RFM). The model was refined by integrating ground
207 control points (GCPs) and consequent improvement of geometric accuracy for orthorectified data.
208 To increase the original geometrical resolution of MS bands (1.24 m), the hyperspherical color space
209 (HCS) resolution merge pan-sharpening algorithm (Padwick et al., 2010) was applied to merging them
210 with the pan band (0.31 m). HCS was used taking into consideration its capability in preserving the
211 original image spectral information (Dahiya et al., 2013; Padwick et al., 2010). Further, a 7×7
212 smoothing filter was applied, followed by the output resampling by means of the nearest neighbor
213 interpolation algorithm.

214

215 **Table 1** - WorldView-3 sensor wavelength bands [nm] and relative ground sample distance [GSD] details (centered
216 wavelength in brackets).
217

Band	Wavelength [nm]	Ground sample distance (GSD) [m]
Panchromatic	450-800	0.31
Coastal blue	400-450 (425)	1.24
Blue	450-510 (480)	
Green	510-580 (545)	
Yellow	585-625 (605)	
Red	630-690 (660)	
Red-edge	705-745 (725)	
NIR-1	770-895 (835)	
NIR-2	860-1040 (950)	

218

219 Classic corrections, i.e. topographic and atmospheric, were then performed using all WV-3 bands (1-
220 8), by means of the atmospheric correction module (ATCOR Workflow) of ERDAS Imagine® 2018.

221 Therefore, the original digital numbers (DNs) were converted into spectral radiance at sensor's

222 aperture (L_A) for correcting to surface reflectance. To calibrate the images, gain and offset calibration
223 values provided with imagery metadata were used (Balthazar et al., 2012; Vanonckelen et al., 2014).
224 ATCOR3 algorithm is based on MODTRAN atmospheric radiative transfer code and allows to set
225 different weather conditions, and solar zenith and azimuth angles. In our case, a rural aerosol model
226 for spring and summer seasons with a visibility distance of 10 km was the applied to four terrain files
227 (slope, aspect, sky view, and shadow cast) obtained from a digital elevation model (DEM) (Richter,
228 1998, 1997) by a modified Minnaert topographic correction that use a set of empirical rules (Richter et
229 al., 2009), considering rugged terrain effects in the correction process. As input, we used a $1\text{ m} \times 1\text{ m}$
230 DEM derived from an aerial LiDAR dataset surveyed in 2011. Finally, an anomaly detection (AD)
231 process was carried out to identify pixels that have a spectral signature markedly different from most
232 other pixel spectra in the image by mean of the orthogonal subspace projection (OSP) as detection
233 method.

234 In order to support the subsequent classification phases adding texture detail to the pixel classifier, a
235 principal component analysis (PCA) spectral transformation was then adopted. A PCA provides a
236 reduction of correlation among bands' reflectance values, by rotating the axes of the original feature
237 space coordinate system to new orthogonal axes (called principal component, PC) maximizing the data
238 variance, therefore making the data more interpretable (Jolliffe, 2002). In order to select the right
239 number of components that account for a high proportion of the data variance, we calculated PCs for
240 all eight WV-3 bands, also obtaining the covariance matrix and the eigenvalues for each of them.
241 Generally, most of the variance is collected in the first three PCs (Richards and Jia, 2006). In our case,
242 we selected the first two PCs considering that for both imagery their account for more than 97% of the
243 data variance (Table 3).

244

245 **3.3 Geographic object-based image analysis (GEOBIA) and tree crown extraction**

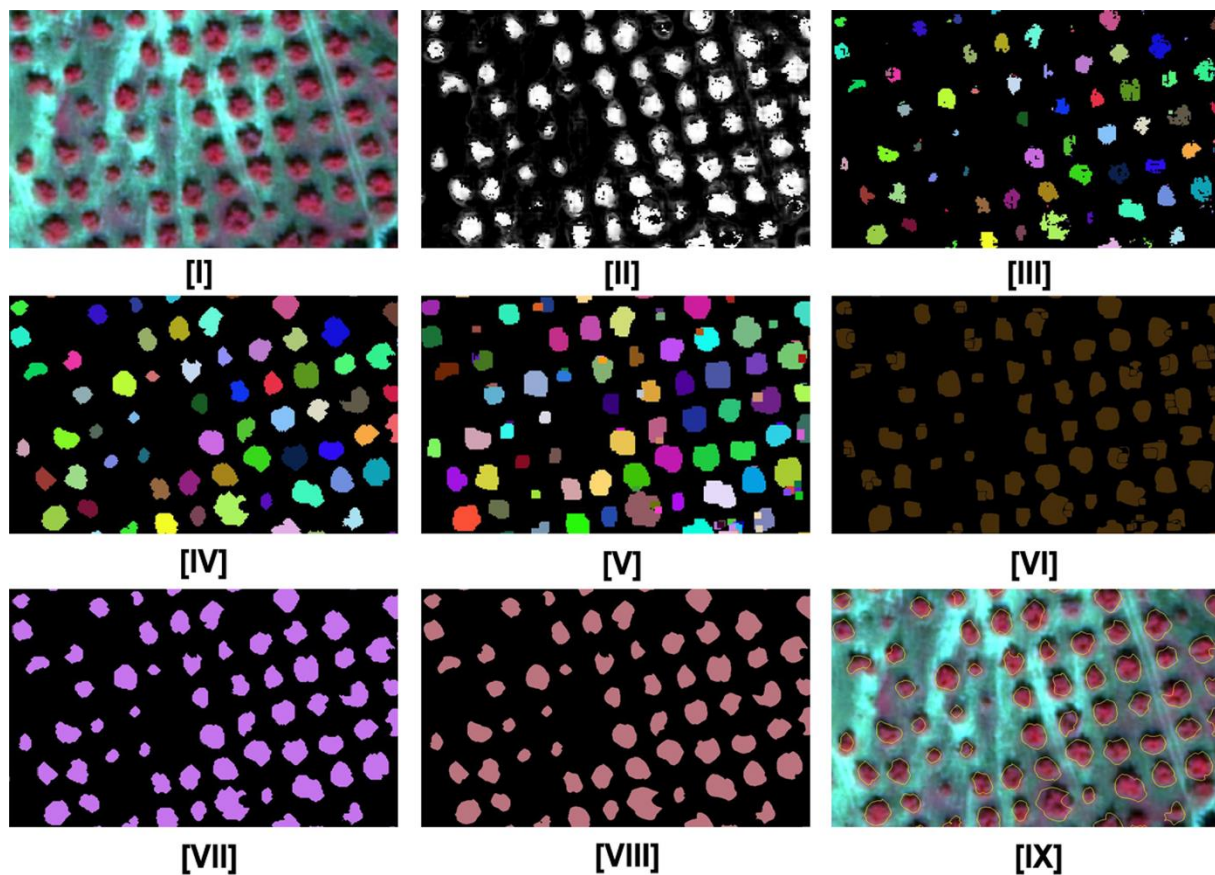
246 The GEOBIA approach was implemented in Erdas Imagine® Objective as semi-automatic process
247 with minimum user intervention, able to extract single olive tree crown and to eliminate the spectral
248 disturbances of background, independently of the plantation pattern. The tree crown model detection

249 was defined with a pixel cue classifier based on multi Bayesian network so that the different output
250 classes could directly interact with each other (Fig. 3). As input data, the atmospherically corrected
251 WV-3 imagery, and the PC1 and PC2 layers were used for both A and B study areas. Preliminarily, for
252 each study area, a set of 30 olive tree crowns representing our feature training reference samples, and a
253 set of background samples, were manually digitized as vector polygons. PC1 and PC2 data layer were
254 added as input to the Identity cue to use as a metric to the Pixel Classifier. Then, a single feature
255 probability (SFP) method was applied to the WV-3 imagery to calculate probability metrics (ranging
256 from 0 to 1) of the input multispectral image, comparing its pixel values with those of the digitized
257 polygons. Higher and lower probability values were assigned to pixels whose values were similar or
258 significantly different from the values of pixels in the non-background training samples, respectively.
259 In the training phase, pixels identified with training polygons belonging to single olive trees were used
260 to compute pixel cue metrics for training the pixel classifier for each study area. The selected pixel
261 were compared, during this process node, to the training pixels obtaining a pixel probability layer (Fig.
262 3) representing the probability in which each pixel's value is an object of interest (i.e. an olive tree
263 crown). Then, a threshold/clump function was applied on the pixel probability layer by keeping only
264 those pixels presenting a percentage probability greater than or equal to the threshold value of 0.95, in
265 our case. Each created raster object is a clump object (i.e., the belonging pixels share a common ID
266 class in the attribute table).

267 Based on a raster object pixel distribution, we set a 5 x 5 circular kernel size to expand the raster
268 object distribution with a minimum object size of 40 pixels, and then specify a minimum clump size of
269 40 pixels. Clumps smaller than the specified number were eliminated. Raster objects were
270 automatically vectorized based on the associated probability metrics and smoothed in shape, applying
271 a smoothing factor of 0.70 (Fig. 3).

272 For each "tree object polygon", size property and a measure of probability membership to the group of
273 tree vector objects was performed by means of an object classifier using training sample distribution
274 parameters such as mean, minimum, maximum and standard deviation values. The automated
275 extraction phase was then performed to measure how closely the selected polygons match the training

276 objects. Objects processed passed through the object cue metrics calculation such as shape (circularity)
277 and size (area) with a pixel probability weight set to 95%.
278



279
280 **Fig. 3.** Geographic object-based image analysis (GEOBIA) sequenced feature model process nodes for the extraction of olive
281 tree crowns. (I): a subset of the corrected WorldView-3 (WV-3) satellite imagery, presented in a false infrared color band
282 combination (RGB 7-5-3); (II): raster pixel processor; (III): raster object creator; (IV-V): raster object operators; (VI): raster to
283 vector conversion; (VII): vector object operator; (VIII): vector object processor; (IX): extracted olive tree crown boundaries
284 [yellow line] overlapped on the input image.
285

286 The process ended with a vector clean-up operation with a probability filter function that removed all
287 vector objects whose zonal probability mean was less than the specified minimum probability by
288 remodeling the existing vector objects (Fig. 3). This value was set to 95%. The resulting vector objects
289 represent the extracted olive tree crowns (Fig. 3).

290

291 **3.4 GEOBIA and tree crown extraction accuracy**

292 To assess the tree crown extraction accuracy, all olive trees' crowns falling in the 8 plots (A₁- A₄ and
293 B₁- B₄) were digitized by on-screen photointerpretation and used as reference data (Erikson, 2004;

294 Larsen et al., 2011; Wang et al., 2004). To ensure the correct geolocalization of each tree falling in the
 295 eight plots, a set of ground control points (ground truths) was defined collecting the position of each of
 296 them by means of a differential GNSS (planimetric accuracy = ±0.05 m). These points were then used
 297 as reference data in the photointerpretation stages display their position on the pan-sharpened WV-3
 298 imagery (Koc-San et al., 2018; Rahman et al., 2018; Robson et al., 2017; Srestasathiern and Rakwatin,
 299 2014). The accuracy was assessed as object-based evaluation by comparing the total number of
 300 correctly detected trees with these reference data. Evaluation was performed by simply counting trees
 301 correctly detected or missing, basing on two independent samples: one for the recall (r) and another
 302 for the precision (p). Recall indicates the omission error while precision indicates the commission
 303 error (Li et al., 2012). The overall accuracy was obtained by the F-score (Eq. 1):

$$304 \quad F\text{-score} = 2 \times \frac{(r \times p)}{(r + p)} \quad (1)$$

305 Where:

$$306 \quad r = \frac{TP}{TP + FN}$$

$$307 \quad p = \frac{TP}{TP + FP}$$

308 F-score represents the harmonic mean of recall and precision and it's a measure of the overall
 309 accuracy (Goutte and Gaussier, 2005; Lu et al., 2014; Sokolova et al., 2006). These performance
 310 indicators were evaluated considering: true positives (TP), i.e. correctly detected trees; false positives
 311 (FP), i.e. erroneously detected trees; and false negatives (FN), i.e. trees not detected.

312 Following the work of Ok et al. (2013), an overlapping threshold of 60% was then defined to assess
 313 the obtained accuracies between the reference and the detected object.

314 To determine the relationship between correctly detected trees and reference data, a regression
 315 analysis was implemented with R statistical software (R Core Team, 2017). The quality of fitted linear
 316 regression model was evaluated based on the coefficient of determination (R^2) and the root mean
 317 square error (RMSE) according to equation 2:

$$318 \quad RMSE = \sqrt{\frac{1}{n} \sum_{i=1}^n (x_i - y_i)^2} \quad (2)$$

319 where, x_i represents reference tree data and y_i the detected tree crown. The significance was also
320 computed.

321 Furthermore, a confusion matrix was used to evaluate the overall 8 plots classification accuracy
322 (Congalton, 1991; Congalton and Green, 2008) obtaining an overall accuracy and the Kappa
323 coefficient (K) as expression of the accuracy in terms of omission/commission errors. To that purpose,
324 in each plot of the two study areas, a set of 10 randomly distributed sample points was defined.

325

326 **3.5 Investigated Vegetation Indices (VIs)**

327 In order to investigate the biophysical characteristics of olive trees, a set of five VIs was defined by
328 selecting those ones (Table 2) based on reflectance bands sensitive to the combined effects of
329 chlorophyll concentration, surface and vegetation canopy architecture. These VIs provide a reliable
330 measure of the photosynthetic material, crucial in understanding the vegetation vigor (Vincini et al.,
331 2008). NDVI, with the normalized combination of its formulation is the most popular VI (Pettoirelli,
332 2013), capable to measure healthy vegetation using the highest chlorophyll absorption and reflectance
333 regions and whose values range from -1 to 1. However, NDVI can saturate in multi-layered dense
334 vegetation, when the leaf area index (LAI) reaches higher values (Haboudane et al., 2004; Maselli et
335 al., 2012; Ortega-Farías et al., 2016; Rouse et al., 1974; Tucker, 1979; Zheng and Moskal, 2009).

336 The modified soil adjusted vegetation index 2 (MSAVI2) is similar to the NDVI, but mitigate the soil
337 background effects. In its first formulation, this was obtained by using an adjustment factor (L), which
338 is a function of the vegetation density and often requires prior knowledge. In the second formulation
339 of the index, instead, the L factor was replaced by a self-regulating factor (Qi et al., 1994). MSAVI2
340 offers good performances with sparse vegetation, where the ground remains particularly visible
341 through the foliage (Eitel et al., 2007; Haboudane et al., 2004; Hunt et al., 2012).

342 NDRE index is a modification of NDVI and its applications include PA, forest monitoring, and
343 identification of vegetation stress (Cammarano et al., 2014; Fitzgerald, 2010; Hunt et al., 2012;
344 Siegmann et al., 2012).

345 NDRE has values ranging from -1 to 1 and differs from NDVI as it uses wavelengths along the Red-
 346 Edge (RE) region. It exploits the vegetation sensitivity to RE to small variations in the canopy foliage
 347 content, the canopy cover degree and senescence.

348

349 **Table 2** - Formulation of the five vegetation indices (VIs) used in the present research.

Index denomination	Index formula*	References
Normalized Difference Vegetation Index (NDVI)	$\frac{(\rho_{NIR1} - \rho_{RED})}{(\rho_{NIR1} + \rho_{RED})}$	(Rouse et al., 1974)
Modified Soil Adjusted Vegetation Index 2 (MSAVI 2)	$\frac{2\rho_{NIR1} + 1 - \sqrt{(2\rho_{NIR1} + 1)^2 - 8(\rho_{NIR1} - \rho_{RED})}}{2}$	(Broge and Leblanc, 2001; Qi et al., 1994)
Normalized Difference Red Edge Vegetation Index (NDRE)	$\frac{(\rho_{NIR1} - \rho_{RedEdge})}{(\rho_{NIR1} + \rho_{RedEdge})}$	(Barnes et al., 2000)
Modified Chlorophyll Absorption Ratio Index Improved (MCARI2)	$\frac{1.5[2.5(\rho_{NIR1} - \rho_{RED}) - 1.3(\rho_{NIR1} - \rho_{GREEN})]}{\sqrt{(2 \times \rho_{NIR1} + 1)^2 - (6 \times \rho_{NIR1} - 5 \times \sqrt{\rho_{RED}})} - 0.5}$	(Haboudane et al., 2004)
Normalized Difference Vegetation Index 2 (NDVI2)	$\frac{(\rho_{NIR2} - \rho_{RED})}{(\rho_{NIR2} + \rho_{RED})}$	(Eckert, 2012; Pu et al., 2012; Wolf, 2012)

350 *in all formulas, ρ is the reflectance at the given wavelength.

351

352 The modified chlorophyll absorption ratio index improved (MCARI2) is one of several CARI indices
 353 identifying the relative abundance of chlorophyll; like MCARI (Daughtry, 2000), it is considered a
 354 good indicator of LAI. It incorporates an adjustment factor for the soil background, while preserving
 355 sensitivity to LAI and resistance to the influence of chlorophyll (Eitel et al., 2007; Haboudane et al.,
 356 2004; Hunt et al., 2012; Main et al., 2011). Thanks to the availability of a NIR2 band, the NDVI2
 357 index (Eckert, 2012; Wolf, 2012) was used as a specific band ratio suitable for WV-3 imagery, which
 358 values range from -1 to 1. Given any other multispectral indices system, a red band and a NIR band
 359 shows the low and high level of vegetation reflectance values, respectively. In the NDVI2, band ratio
 360 between the red coupled with the NIR2 band, which has a higher value than traditional broad NIR
 361 bands, should produce higher NDVI values (Ng et al., 2017; Wolf, 2012).

362 As described, VIs maps for the two study-areas were obtained in the spatial modeler environment in
363 Erdas Imagine® 2018 suite, applying the standard formulations (Table 2) and masking them to the
364 geographical extent of each study area (Fig. 2). Final maps were built in QGIS 3.4 Madeira (Fig. 5-6).

365 **3.6 Statistical Analysis of olive tree spectral signature and derived VIs**

366 To corroborate research findings and further considerations, a statistical analysis was applied to all
367 calculated VIs. To this end, analyses were performed on all extracted VIs within the defined 8 plots
368 (A₁- A₄ and B₁- B₄) using the extracted tree crown vector derived from GEOBIA, in order to separate
369 the real cultivated areas from other parts (Fig. 3). For each plot, all trees falling inside were chosen as
370 statistic samples and, for each crown, basic statistics of VIs values (i.e., mean and standard deviation)
371 were calculated. The mean spectral signature of each plot was also computed and correlation among
372 bands was estimated by a correlation matrix. Single band reflectance values were evaluated using box
373 and whisker plots. Significance was computed using a two-tailed t test with n-2 degrees of freedom.
374 Aiming to assess how suitable VIs are to describe crops condition, we were interested in identifying
375 the regions of the EM spectrum in where olive trees most differ from each other, so that the index can
376 be representative of a real growth condition. For this purpose, one-way analysis of variance (ANOVA)
377 test was used to verify the statistical difference between trees in mean reflectance value in each
378 waveband and in each plot. The ANOVA tested the following hypothesis:

$$379 \quad H_0 = \rho_1 = \rho_2 = \dots \rho_n$$

$$380 \quad H_1 = \text{Not all } \rho_n(i) \text{ are equal}$$

381 where ρ_n represents the mean reflectance of the n-th tree ($n = 1, 2, 3, \dots 13$) and i denotes the
382 waveband. Rejection of the null hypothesis (H_0) indicates the wavebands, at a 95% (p-value <0.05)
383 confidence level, in which the spectral signature differs statistically. H_0 rejection was followed by
384 pairwise multiple comparisons with the post-hoc Tukey HSD test. By counting the number of pairs
385 whose differences are statistically significant on each waveband, it is possible to identify the spectral
386 regions where the olive trees most differ, evidencing the wavebands that may have high discriminative
387 effects on VI's value. First, normality and homoscedasticity (i.e., homogeneity of variances) of the
388 reflectance values across each waveband were verified with Levene's test and Shapiro-Wilk test.

389 Where Levene's test was significant (i.e., it showed unequal variances), then the unequal-variance
 390 (Welch F test) version of ANOVA (Moder, 2010) and the non-parametric Kruskal Wallis test for
 391 taking control of values with non-normal distribution, were used. In these last cases, a Mann-Whitney
 392 *U* test (Zar, 1996) was used as post-hoc pairwise comparison. Statistical analyses were performed with
 393 R statistical software (R Core Team, 2017).

394

395 4. Results

396 4.1 GEOBIA classification accuracy

397 As described in paragraph 3.4, all olive trees' crowns falling in the 8 plots (A₁- A₄ and B₁- B₄) were
 398 digitized by on-screen photointerpretation, thus representing our reference data, and compared to those
 399 extracted by means of GEOBIA classification. To digitize these reference data, the image band
 400 composition which proved to be as the most effective in revealing contrast and properties that were not
 401 visually evident from the other false colors image was the RGB 7-6-5 (NIR1, Re, R) (Fig. 4).

402 The PCA analysis showed that the PCs axis derived from all for all the WV-3 bands, which explain
 403 >95% of the variance (cumulative proportion of all components) were represented by PC1 and PC2 for
 404 a total variance percentage of 97.4 in A and 98.5 in B (Table 3), such that only these two components
 405 were used in GEOBIA tree crown classification process.

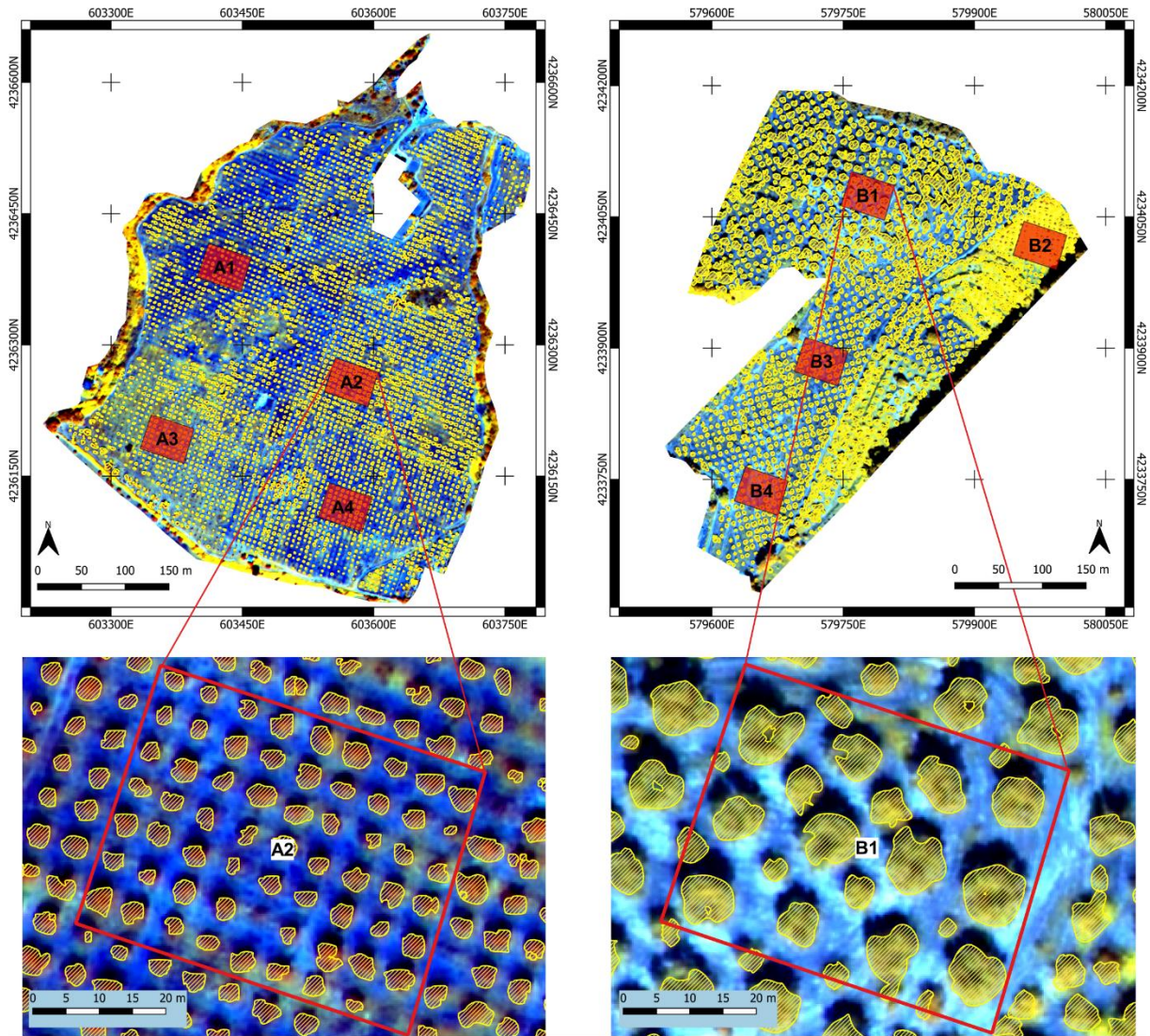
406

407 **Table 3** - Results of principal component analysis (PCA) of WV-3 imagery of study areas A and B, showing the Eigenvalues
 408 obtained from the covariance matrix and the percentage variance contribution of each principal component (PC).

PC	A			B		
	Eigenvalue	%Variance	Cumulative Variance	Eigenvalue	%Variance	Cumulative Variance
1	25455.122	61.22	61.22	60209.084	80.56	80.56
2	15025.964	36.14	97.36	13390.535	17.92	98.48
3	469.852	1.13	98.49	541.596	0.72	99.20
4	256.930	0.62	99.18	361.990	0.48	99.68
5	200.421	0.48	99.66	151.383	0.20	99.88
6	123.278	0.30	99.96	49.487	0.07	99.95
7	41.494	0.03	99.99	29.601	0.04	99.99
8	8.666	0.01	100	7.745	0.01	100

409

410



Legend

- Plots for accuracy assessment
- Detail of plots A2 and B1
- Olive tree crowns

Coordinate reference system (CRS)
WGS84-ETRF89 UTM 33 (EPSG code 25833)

411

412 **Fig. 4.** WV-3 scene subset of the two olive orchards (acquisition date: [A] 24 June 2016; [B] 2 July 2016) showed with
 413 vegetation enhancement color band combination (RGB 7-6-5). In each study area, in red, are highlighted the four plots
 414 defined for accuracy assessment of geographic object-based image classification (GEOBIA) and for statistical analyses of
 415 spectral behavior of olive trees [Top left, study area A. Top right, study area B. Down left and down right, image detail of
 416 plot A2 and B1, respectively, with superimposed (in yellow) the polygonal boundaries of tree crowns obtained through
 417 GEOBIA classification and extraction].

418

419 Results showed that most of the trees were correctly classified and extracted in all plots of both study
 420 areas. The accuracy assessment showed an overall accuracy of 95% in study area A and 98% in study
 421 area B (Table 4). The final object probability layer, in which each pixel's value represents the
 422 probability that it is the feature of interest, reached the probability value of 82% in study area A and

423 78% in study area B. Crown dimensional analysis confirmed a marked difference on tree structure
 424 between study areas, with a more vigorous structure in olive orchard B.

425

426 **Table 4** - Accuracy assessment of classified study area images derived from GEOBIA and olive sample trees cue metrics [(±
 427 n): ± st.dev].

Sample plot	Pixel probability	Area [m ²]	Circularity	Probability
A ₁	0.70 (±0.07)	2.50 (±1.27)	0.81 (±0.07)	0.76 (±0.11)
A ₂	0.78 (±0.06)	6.51 (±1.58)	0.79 (±0.07)	0.82 (±0.11)
A ₃	0.78 (±0.09)	4.54 (±2.40)	0.84 (±0.08)	0.89 (±0.12)
A ₄	0.80 (±0.06)	5.27 (±1.37)	0.80 (±0.07)	0.83 (±0.11)
<i>Overall plot accuracy (%)</i>	95.33			
<i>Overall plot K coefficient</i>	0.9513			
B ₁	0.73 (±0.09)	31.10 (±19.08)	0.80 (±0.08)	0.83 (±0.15)
B ₂	0.54 (±0.08)	11.20 (±6.16)	0.75 (±0.08)	0.73 (±0.12)
B ₃	0.75 (±0.08)	16.48 (±7.05)	0.76 (±0.08)	0.78 (±0.12)
B ₄	0.74 (±0.08)	14.55 (±7.35)	0.87 (±0.07)	0.79 (±0.13)
<i>Overall plot accuracy (%)</i>	98.67			
<i>Overall plot K coefficient</i>	0.9724			

428

429 The total number of olive trees in the 8 plots were 359, 347 of which were correctly extracted, missing
 430 11 trees and falsely detecting 1 tree (Table 5). In study area A, characterized by smaller olive trees,
 431 values of r (omission error) varies from 0.91 to 0.98 (overall value 0.95) while p value (commission
 432 error) is 1. The F-score, which considers both r and p, varies from 0.95 to 0.99 (overall value of 0.97).
 433 Whereas in study area B, with larger olive trees, value of r ranges from 0.95 to 1 (overall value of
 434 0.97). The value of p is 1 in every plot except B2 (overall value of 0.97). The F-score ranges from 0.96
 435 to 1 (overall value of 0.98). According to the obtained results, in plots B3 and B4 the best detection
 436 rate at 100% was obtained, whilst plot A1 showed the worst detection rate (91.2%).

437 Very small trees (i.e., crown diameter <2 m) often tend to show a higher number of FN pixels because
 438 part of their surrounding background is not included in the tree crown. This explains the decrease in
 439 the accuracy obtained in plot A1 (F-score = 0.95), despite the promising success level for r (≈0.9). As
 440 expected, large tree crowns tend to be more precisely detected. In some cases however, although very
 441 small trees with a tree crown area (TCA) of 0.096 m² (9 pixels) were also correctly extracted, this
 442 procedure tends to loose portions of them or, depending on their shape, divides them into two or more
 443 objects (Fig. 3). The relationship between the number of reference trees and the number of extracted

444 trees for each plot are shown in Fig. 4. The relationship between the number of reference trees and the
 445 number of extracted trees for each plot are shown in Fig. 5. The correlation result is relatively strong
 446 with $R^2 = 0.986$ and $RMSE = 1.36$, (p -value < 0.001).

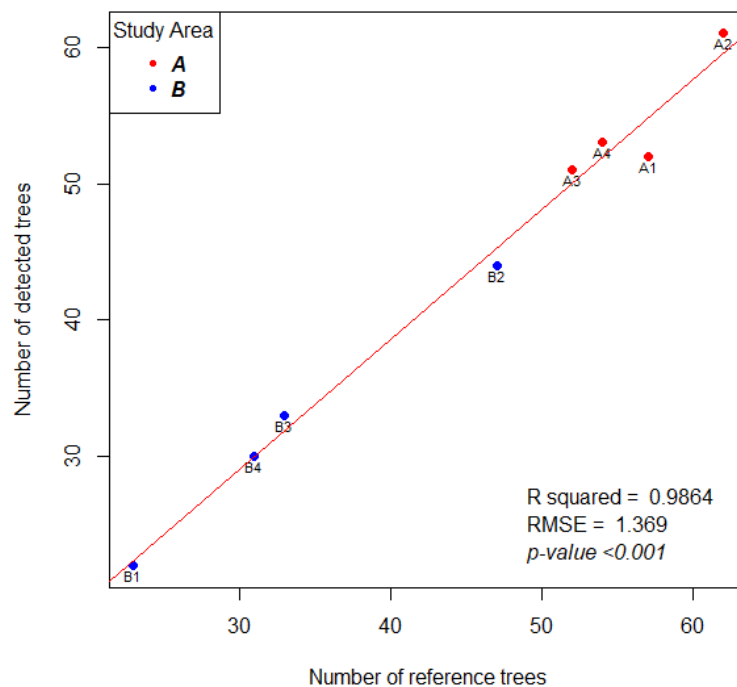
447

448 **Table 5** - Results and accuracy indicators of the olive tree crown extraction (TP, true positive; FP, false positive; FN, false
 449 negative; r , recall; p : precision).

Plot ID	Number of trees	Number of detected trees	TP	FP	FN	r	p	F-score	Rates (TP/n° trees) [%]
<i>A₁</i>	57	52	52	0	5	0.91	1.00	0.95	91.2
<i>A₂</i>	62	61	61	0	1	0.96	1.00	0.98	98.4
<i>A₃</i>	52	51	51	0	1	0.98	1.00	0.99	98.1
<i>A₄</i>	54	53	53	0	1	0.98	1.00	0.99	98.1
Overall A	225	217	217	0	8	0.95	1.00	0.97	96.4
<i>B₁</i>	23	22	22	0	1	0.95	1.00	0.97	95.6
<i>B₂</i>	47	44	44	1	2	0.95	0.97	0.96	93.6
<i>B₃</i>	33	33	33	0	0	1.00	1.00	1.00	100
<i>B₄</i>	31	31	31	0	0	1.00	1.00	1.00	100
Overall B	134	130	130	1	3	0.97	0.99	0.98	97.3
Overall	359	347	347	1	11	0.96	0.99	0.97	96.8

450

451



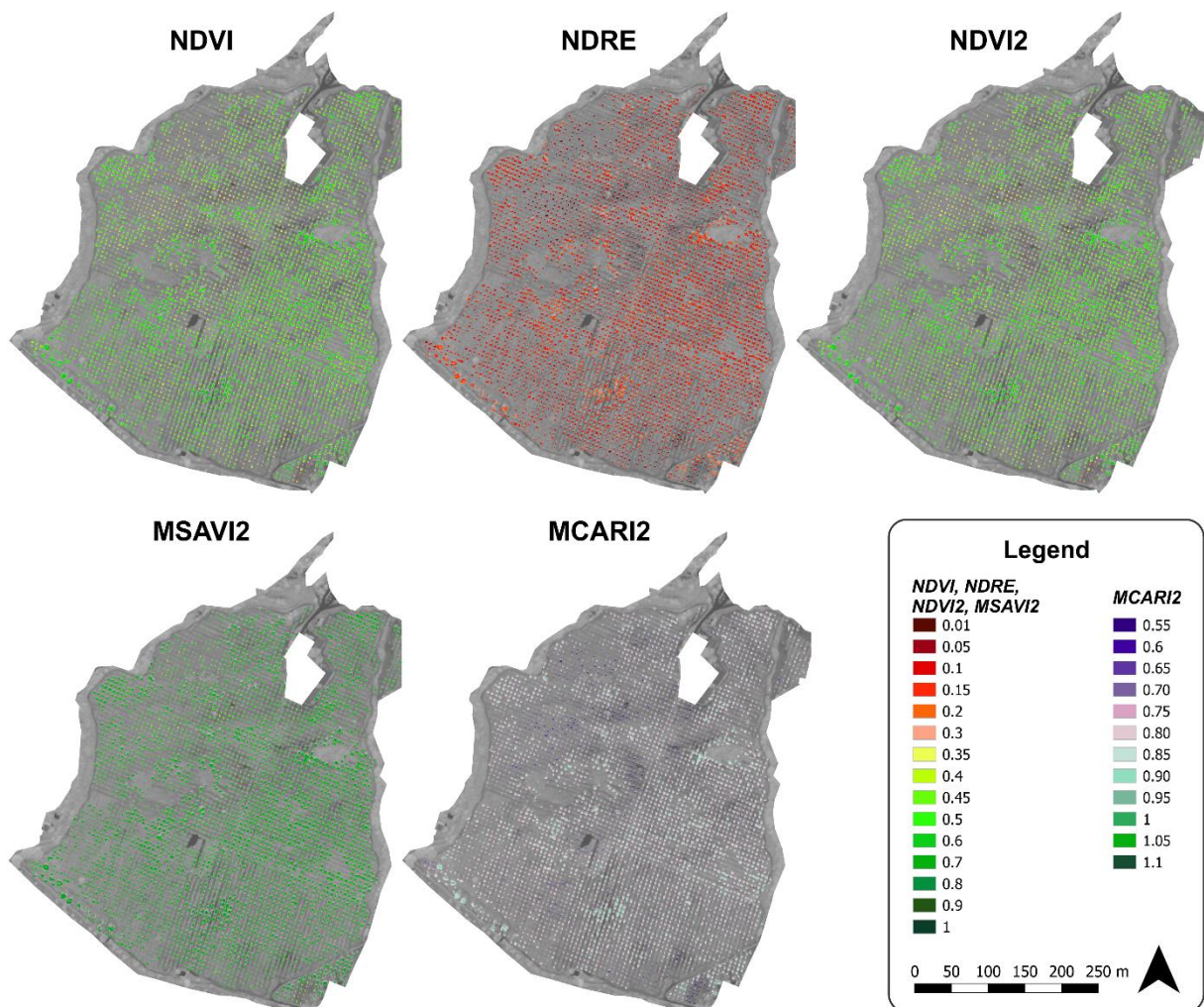
452

453 **Fig. 5.** Relationship between number of reference trees and number of correctly detected trees in the eight investigation plots.
 454

455 **4.2 Vegetation indices (VIs) maps**

456 For both study areas, the spatial distribution of NDVI, MSAVI2, NDRE, MCARI2, and NDVI2
457 already showed significant pattern, i.e. zones with negative behavior are well recognizable (Fig. 6
458 and 7). However, all VIs maps were clearly affected by crown shadows of olive trees, and even small
459 changes in elevation of the terrain and herbaceous/shrub vegetation. At border zones of A olive
460 orchard, some continuous green pixels often appear, representing positive values of the indices, due to
461 the different oaks vegetation surrounding the olive orchard with continuous canopy cover. In B, some
462 areas where vegetation shows good values for all VIs are also discriminable in the field. These
463 features were well differentiated in the VIs color images.

464



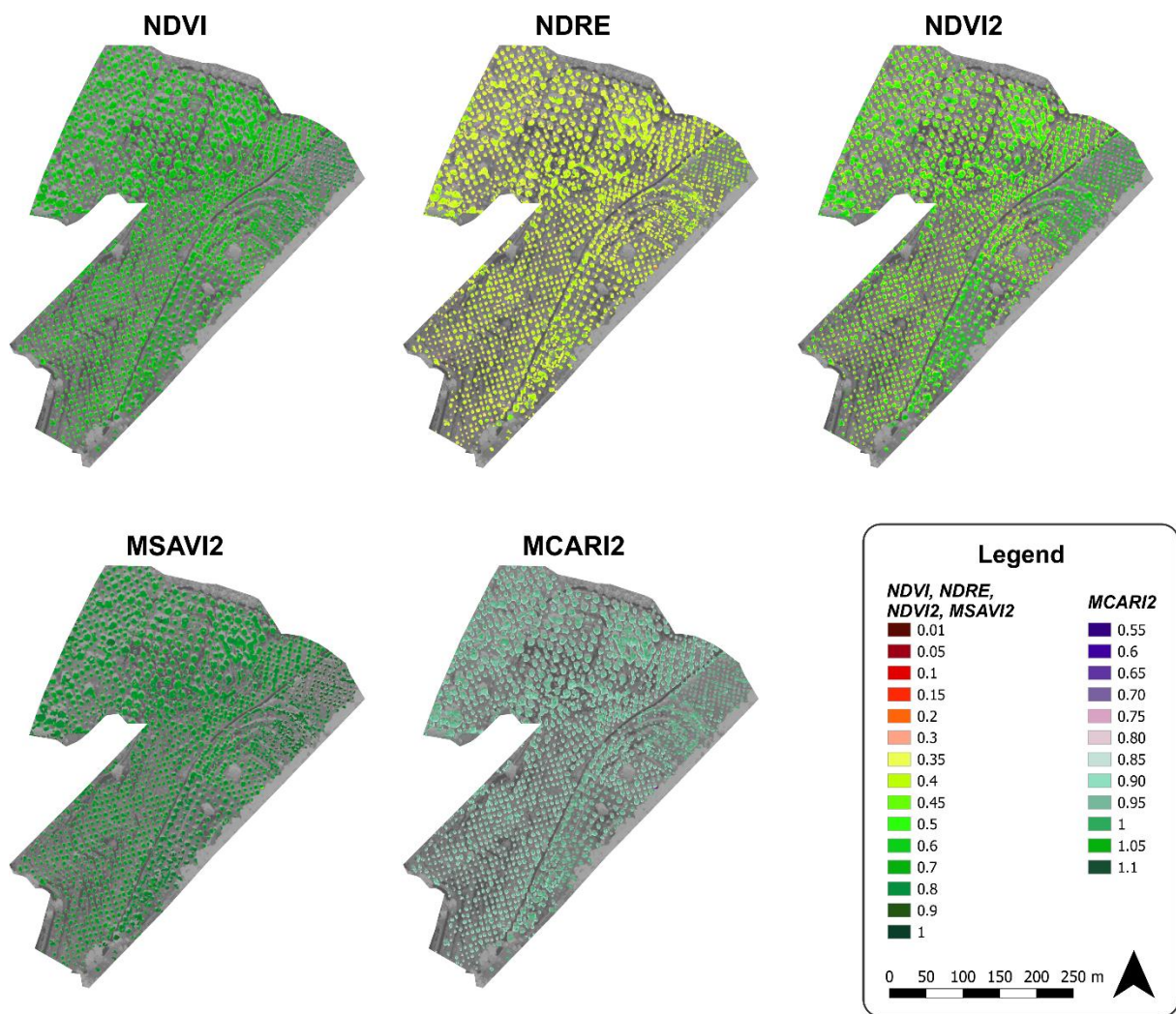
465

466 **Fig. 6.** Vegetation indices (VIs) maps of study area A

467

468 To confirm these qualitative considerations and to mitigate the effect of soil and herbaceous layer
 469 background, statistical analyses were performed in the eight plots at tree crown detail, using the
 470 derived GEOBIA tree crowns polygons as statistical unit (Table 5). For each plot, basic statistics of
 471 indices values showed a different behavior of vegetation. In particular, the mean index value reflects a
 472 mean productivity and biomass, whereas the standard deviation represents a measure of the spatial
 473 variability in productivity (Rouse et al., 1974).
 474 The mean value for all indices in study area A suggested that health condition of plot A₂, A₃ and A₄ is
 475 better than A₁, as well as in study area B health condition of plot B₃, B₄ and B₂ is better than in plot B₁,
 476 respectively. Concerning the NDVI, mean value ranges between 0.45 and 0.54 in A and between 0.62
 477 and 0.77 in B showing higher level of biomass in the latter case.

478



479

480 **Fig. 7.** Vegetation indices (VIs) maps of study area B

481 The increase in the mean value of MSAVI2, able to suppress the effects of soil background, is
 482 approximately 25% in each plot, with the minimum increase of 19% in plot A2 and A4 and the
 483 maximum of 27% in plot A1.
 484 In B, the increase of MSAVI2 mean value is approximately of 17%, with the minimum increase of
 485 12% in plot B2 and the maximum of 19% in plots B1 and B4. Given that the reflectance in RE band is
 486 higher than in the red one, NDRE shows different value ranges compared to those of NDVI. The
 487 NDRE reaches the maximum value in plots A2 and B2, whereas the minimum in plots A1 and B1
 488 (Table 6), depending also on different foliage cellular structure.
 489 The same behavior was found finally for MCARI2 and NDVI2 that prove again a situation similar to
 490 the previous findings regarding the consistence of chlorophyll concentration.

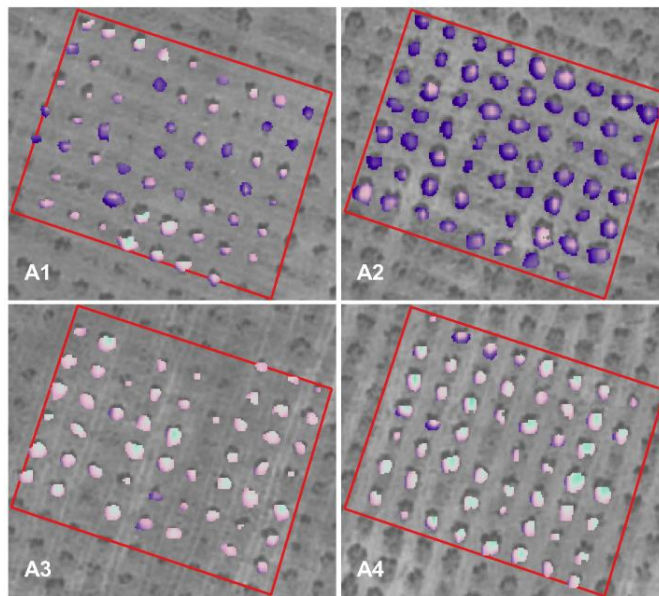
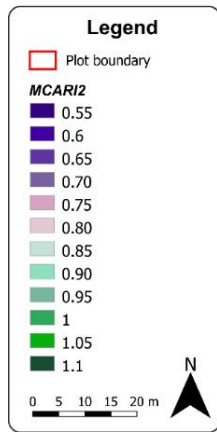
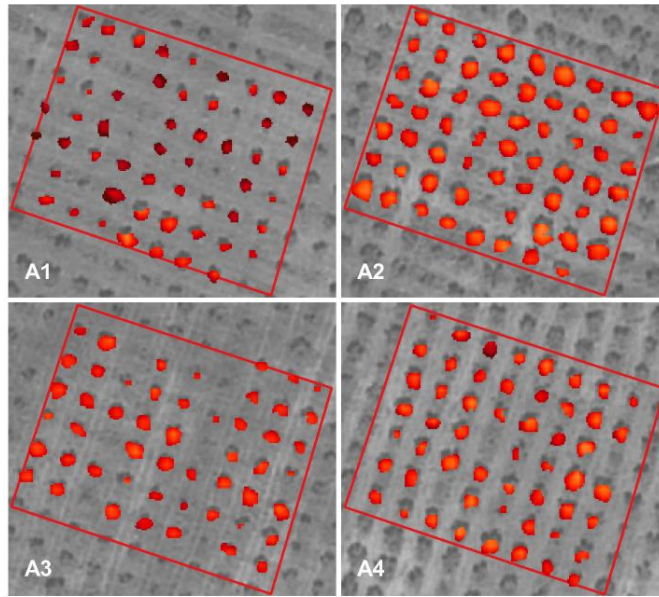
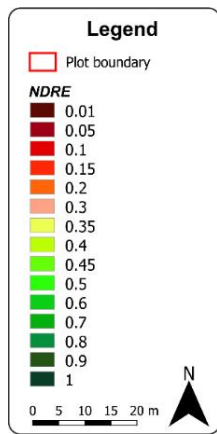
491

492 **Table 6** - Univariate statistics of Vegetation indices (VIs) map values, for each plot, inside A and B study areas

Study area	Plot	NDVI		MSAVI2		NDRE		MCARI2		NDVI2	
		Mean	± st.dev	Mean	± st.dev	Mean	± st.dev	Mean	± st.dev	Mean	± st.dev
A	A ₁	0.45	0.03	0.62	0.03	0.12	0.02	0.77	0.03	0.49	0.03
	A ₂	0.55	0.03	0.68	0.03	0.15	0.02	0.82	0.02	0.54	0.03
	A ₃	0.54	0.02	0.68	0.01	0.14	0.02	0.80	0.02	0.53	0.02
	A ₄	0.54	0.03	0.67	0.02	0.13	0.02	0.81	0.02	0.53	0.02
B	B ₁	0.62	0.02	0.77	0.01	0.38	0.02	0.93	0.02	0.48	0.02
	B ₂	0.77	0.02	0.88	0.02	0.43	0.02	0.97	0.01	0.68	0.03
	B ₃	0.63	0.02	0.77	0.01	0.39	0.02	0.92	0.01	0.49	0.03
	B ₄	0.63	0.02	0.78	0.01	0.39	0.02	0.92	0.01	0.49	0.03

493

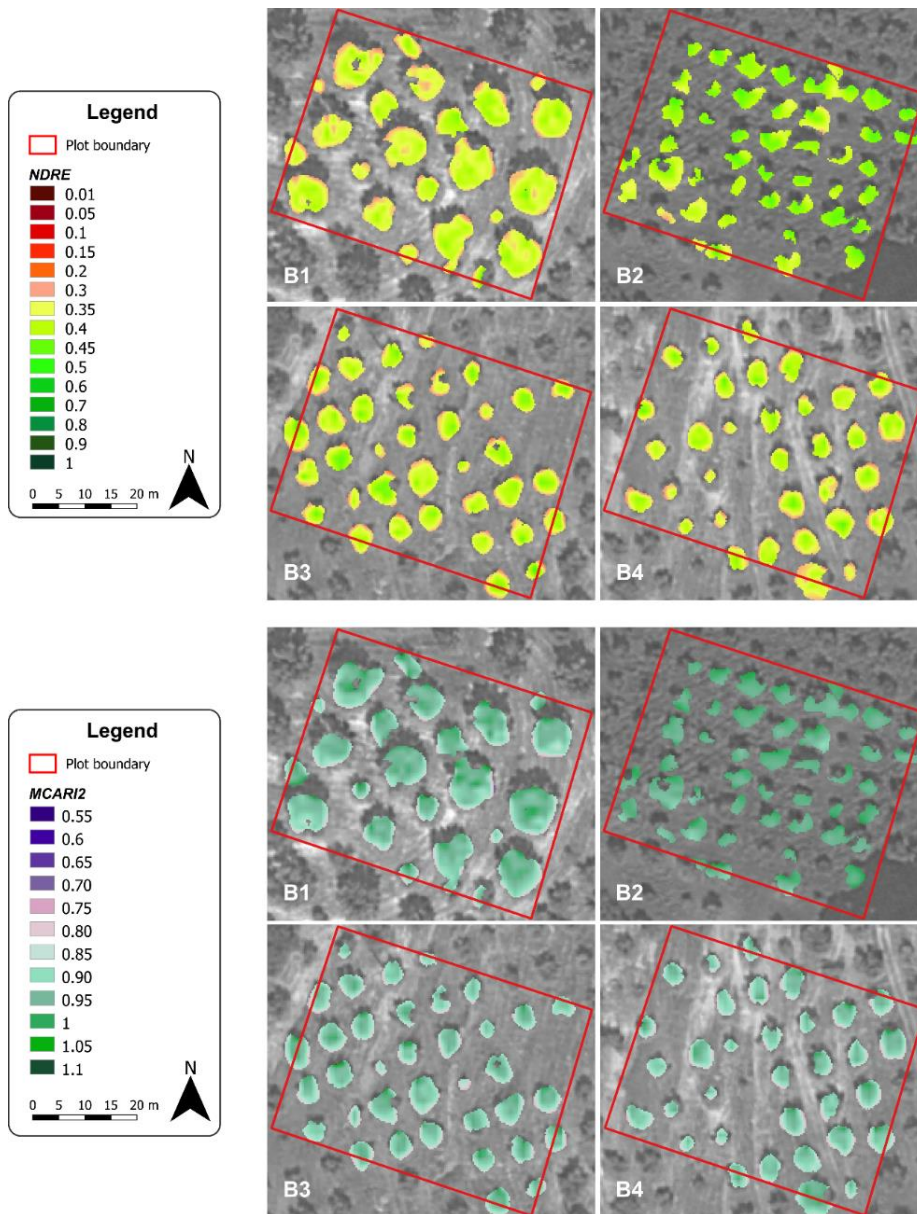
494 However, considering that previous statistic parameters are not able to fully describe data
 495 distributions, the relative frequency distribution of VIs values was calculated for each plot at tree
 496 crown detail (Figg. 8-9). To show an example of how structural vigor and chlorophyll concentration
 497 vary among different plots, we compared NDRE and MCARI2 values' distribution of single tree
 498 crown of the two study areas. Single tree crown VI of the plots confirmed that the trees of study area
 499 A have a worse vegetative state than those in study area B. For all the VI maps, the graphics show that
 500 the pixels belonging to area A are distributed over VI values lower than in area B, confirming again
 501 the previous findings.



502

503 **Fig. 8.** Maps of Normalized Difference Red Edge (NDRE) and Modified Chlorophyll Absorption Ratio Index Improved
 504 (MCARI2) Vegetation indices (VIs) at tree crown detail of study area A.
 505

506 Considering only NDRE, all the plots in the study area B reach the highest values, denoting a major
 507 structural vigor than those in study area A, trees differing mostly in crown dimension between the two
 508 study areas. Likewise, in B the MCARI2 values appear as higher than in A. The decrease of the values
 509 of MCARI2 in A may not be directly related to the state of health only but to the whole trees structures
 510 in the relative plots. This consideration is supported by the assessment made in the previous analysis,
 511 referring it to the only NDRE pixels value.

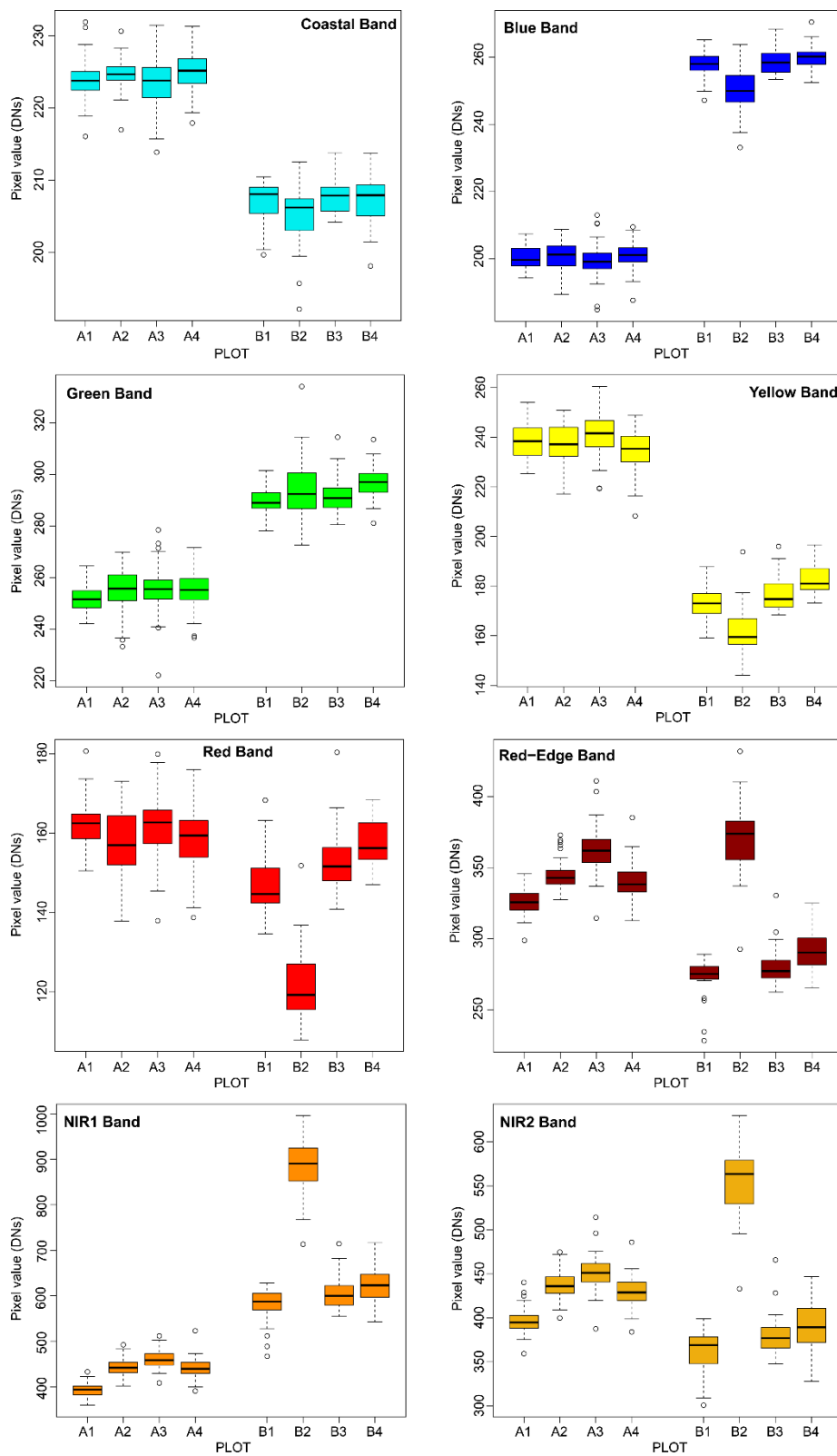


512
 513 **Fig. 9.** Maps of Normalized Difference Red Edge (NDRE) and Modified Chlorophyll Absorption Ratio Index Improved
 514 (MCARI2) Vegetation indices (VIs) at tree crown detail of study area B
 515

516 **4.3 Tree crown extraction and spectral behavior**

517 A comparative analysis of the spectral properties revealed that most of the olive trees had similar
 518 spectral intra-plot patterns. Most of the spectral variability is visible from the RE to NIR2 band while
 519 the peak of reflectance was reached at RE band (Fig. 10). On the other hand, NIR values showed a
 520 different range of reflectance spectra. The maximum reflectance was obtained in the NIR1 and NIR2
 521 bands in B (Fig. 10). Analyzing these differences, and representing them according to the mean single

522 band reflectance values using box and whisker plots (Fig. 10), it was possible to better understand how
 523 spectral signature changes between the eight plots.



524
 525 **Fig. 10.** Box-and-whisker plots of single WV-3 bands reflectance values variability in each study area plot (A1-A4 and B1-
 526 B4).
 527

528 About coastal and blue band in A, an overall low variability was found whilst highest values in the
 529 green band confirmed major reflection in this region of the EM spectrum. In the Yellow band, the
 530 highest pixel value was reached in plot A₃ that had the highest value in the RE, NIR1 and NIR2 band
 531 too. RE, NIR1 and NIR2 reflectance peaks were reached in plot A₃ and A₂, confirming the best
 532 vegetative state of olive trees that fall in to these plots, with the lowest reflectance in A₁ and A₄ in each
 533 of these bands.

534 In general, the shape and distribution toward the spectral value is flat for all plots, with a minimal
 535 green and yellow peak and different distribution patterns across 705-1040 nm wavelength. Differently,
 536 in B coastal and yellow bands showed lower pixel value in these EM regions compared to A plots,
 537 with highest values in the green and blue band. A similar distribution pattern is visible in the red band
 538 with the lowest peak in plot B₂. The RE, NIR1 and NIR2 peak reflectance was reached in plot B₂
 539 almost confirming a marked best vegetative state of the olive trees, with the lowest reflectance in B₁
 540 in each of these bands. In principle, each B plot seems to display leaves with high photosynthetic
 541 capacity to maximize direct beam radiation, resulting in higher NIR values.

542 Based on the correlation matrix, computed from the reference sample trees (Tables 7 and 8), it is
 543 possible to identify some correlations between bands. For both study areas, the correlation among RE,
 544 NIR1 and NIR2 bands was highly significant. In B it was found significant correlations also between
 545 Yellow, Blue, Red and Coastal blue band. Within each group, correlations among bands are quite high
 546 with an overall low *p*-value. Thus, these bands could provide redundant information.

547

548 **Table 7** - Pairwise correlations among the eight bands of WorldView-3 (WV-3) imagery, computed from the reference
 549 sample trees of study area A. Correlation values are given in the lower triangle of the matrix, and the two-tailed probabilities
 550 are given in the upper (Correlations >0.75 in bold letters, ns: no significance; **p*<0.01, ***p*<0.05).

A / Band	Coastal blue	Blue	Green	Yellow	Red	Red-edge	NIR-1	NIR-2
Coastal blue	-	ns	ns	**	ns	ns	ns	ns
Blue	0.93	-	ns	ns	ns	ns	ns	ns
Green	0.20	-0.10	-	ns	ns	ns	**	ns
Yellow	-0.94	-0.90	-0.06	-	ns	ns	ns	ns
Red	-0.84	-0.64	-0.52	0.69	-	ns	ns	ns
Red-edge	-0.39	-0.65	0.81	0.40	-0.15	-	ns	**
NIR-1	-0.02	-0.33	0.97	0.18	-0.41	0.94	-	*
NIR-2	-0.10	-0.44	0.94	0.22	-0.31	0.97	0.99	-

551

552 **Table 8** - Pairwise correlations among the eight bands of WorldView-3 (WV-3) imagery, computed from the reference
 553 sample trees of study area B. Correlation values are given in the lower triangle of the matrix, and the two-tailed probabilities
 554 are given in the upper (Correlations >0.75 in bold letters, ns: no significance; *p<0.01, **p<0.05).

B Band	<i>Coastal blue</i>	<i>Blue</i>	<i>Green</i>	<i>Yellow</i>	<i>Red</i>	<i>Red-edge</i>	<i>NIR-1</i>	<i>NIR-2</i>
<i>Coastal blue</i>	-	ns	ns	ns	**	ns	ns	ns
<i>Blue</i>	0.96	-	ns	**	*	ns	ns	**
<i>Green</i>	-0.09	0.02	-	ns	ns	ns	ns	ns
<i>Yellow</i>	0.89	0.98	0.15	-	*	ns	ns	ns
<i>Red</i>	0.92	0.97	0.12	0.98	-	ns	ns	ns
<i>Red-edge</i>	-0.91	-0.85	0.25	-0.80	-0.85	-	*	*
<i>NIR-1</i>	-0.91	-0.92	0.20	-0.83	-0.87	0.98	-	*
<i>NIR-2</i>	-0.91	-0.90	0.32	-0.84	-0.91	0.98	0.99	-

555

556 **4.4 Spectral ANOVA test**

557 In each plot, differences in spectral values between every single wavelength of sample trees were
 558 tested with one-way ANOVA. Results show significant differences among Yellow, Red, RE, NIR1
 559 and NIR2 band in each plot study area A (Table 8). In B, results show significant differences in
 560 reflectance values between all bands in almost all plots, with the maximum of differences in RE, NIR1
 561 and NIR2 bands (Table 10).

562 Referring to study area A, post-hoc tests (Tukey HSD, Mann-Whitney) emphasized that red spectral
 563 region was significantly different in the following plots comparison: A₁/A₂, A₁/A₄, A₃/A₄ (Table 9).
 564 The obtained spectral behavior of NIR1 and NIR2 revealed that such differences were statistically
 565 significant for a higher number of plots (Table 9).

566 **Table 9** - Summary of normality, homoscedasticity tests and ANOVA statistics result of all grouped band reflectance value,
 567 among all A plots. Summary of post-hoc test for significant band comparison [ns: no significance; different letters indicate
 568 the different plots where single band reflectance values significantly differ (p < 0.05)].

Band	Wavelength [nm]	Levene's test (p-value)	Shapiro-Wilk (W)	F	Welch test (F)	Kruskal Wallis (H)	Tukey HSD test (Q)	Mann-Whitney (U)
<i>C. blue</i>	400-450	0.003	0.974*		1.57	7.80	ns	
<i>Blue</i>	450-510	0.335	0.971	1.00			ns	
<i>Green</i>	510-580	0.355	0.985	1.34			ns	
<i>Yellow</i>	585-625	0.713	0.981	4.82*			A ₃ /A ₄	
<i>Red</i>	630-690	0.188	0.991	3.59*			A ₁ /A ₂ , A ₁ /A ₄ , A ₃ /A ₄	
<i>Red-edge</i>	705-745	0.032	0.973*		45.2*	89.50*		A ₁ /A ₂ , A ₁ /A ₄ , A ₂ /A ₃ , A ₃ /A ₄
<i>NIR1</i>	770-895	0.865	0.993	71.6*			A ₁ /A ₂ , A ₁ /A ₃ , A ₁ /A ₄ , A ₂ /A ₃ , A ₃ /A ₄	

NIR2	860-1040	0.753	0.994	56.4*			A ₁ /A ₂ , A ₁ /A ₃ , A ₁ /A ₄ , A ₂ /A ₃ , A ₃ /A ₄	
-------------	----------	-------	-------	-------	--	--	---	--

569 *marked value are where spectral signatures differ statistically for p -value <0.05

570
571
572
573

Table 10. Summary of normality, homoscedasticity tests and ANOVA statistics result of all grouped band reflectance value, among all B plots. Summary of post-hoc test for significant band comparison [ns: no significance; different letters indicate the different plots where single band reflectance values significantly differ ($p < 0.05$)].

Band	Wavelength (nm)	Levene's test (p-value)	Shapiro-Wilk (W)	F	Welch test (F)	Kruskal Wallis (H)	Tukey HSD test (Q)	Mann-Whitney (U)
C. blue	400-450	0.053	0.972	3.14*			B ₂ /B ₃	
Blue	450-510	0.173	0.963	32.0*			B ₁ /B ₂ , B ₂ /B ₃ , B ₂ /B ₄	
Green	510-580	0.015	0.975*		7.12*	15.18*		B ₁ /B ₄ , B ₃ /B ₄
Yellow	585-625	0.174	0.942	49.8*			B ₁ /B ₂ , B ₂ /B ₃ , B ₁ /B ₄ , B ₁ /B ₃	
Red	630-690	0.532	0.923	155.2*			B ₁ /B ₂ , B ₁ /B ₃ , B ₁ /B ₄ , B ₂ /B ₃ , B ₂ /B ₄	
Red-edge	705-745	0.007	0.981*		168.0*	93.02*	B ₁ /B ₂ , B ₁ /B ₄ , B ₂ /B ₃ , B ₂ /B ₄ , B ₃ /B ₄	
NIR1	770-895	0.020	0.993*		267.4*	88.77*		B ₁ /B ₂ , B ₁ /B ₄ , B ₂ /B ₃ , B ₃ /B ₄ ,
NIR2	860-1040	0.000	0.985*		218.3*	85.69*		B ₁ /B ₂ , AC, B ₁ /B ₄ , B ₂ /B ₃ , B ₂ /B ₄

574 *marked value are where spectral signature differ statistically for p -value <0.05

575

576 There was only one statistically significant differences between plots A₃:A₄ in the yellow wavelength
577 value. In study area B, post-hoc tests showed a higher number of plot pairs that were statistically
578 different in the whole spectrum region (Table 10), confirming the heterogeneous behavior of all olive
579 trees between plots.

580

581 5. Discussion

582 The reliability of WV-3 data has been thoroughly tested and confirmed by the high overall accuracies
583 of the obtained results, thanks to their high spectral, radiometric and spatial resolution. Due to the high

584 geometrical resolution of WV-3 imagery, it was possible to perform an overall accurate olive tree
585 crown extraction and derive VIs maps that cancel or diminish the effect of soil brightness as in cases
586 where vegetation is sparse and the pixels in the image are a combination of vegetation and soil
587 information (Huete, 1988). In our proposed methodology, olive tree canopy boundaries extracted via
588 GEOBIA procedure, provided good results with an overall tree detection rate greater than 95% ($R^2 =$
589 0.98). Although several studies have reported the identification and extraction of TCA for other fruit
590 crop type with WV imagery (Anderson et al., 2018; Rahman et al., 2018; Robson et al., 2017), our
591 proposed semiautomatic procedure of detection and extraction of olive TCA provided a close to real
592 canopy shape boundary, if compared to the abovementioned works. Our findings showed that our
593 methodology allowed to correctly detect and extract very small olive trees with a TCA of 0.096 m²
594 (corresponding to nine pixels).

595 Olive orchard mapping reaches a high overall accuracy with high kappa coefficient values in both
596 study areas (Table 5) especially when compared with other studies that used the same sensor, both in
597 the general classification of a scene as well as on the identification of individual objects (Han et al.,
598 2017; Johnson et al., 2017; Koenig and Gueguen, 2016; Majid et al., 2016; Srestasathien and
599 Rakwatin, 2014; Ye et al., 2017). Nevertheless, as can be observed in the subplot details (figg. 8 and
600 9), our implemented procedure tends to loose portions of them or, depending on their shape, divides
601 them into two or more objects.

602 On the other hand, our results are in line with those reported in researches based on other types of
603 VHR images (Aguilar et al., 2013, 2016; Alrassi et al., 2016; Gaertner, 2017; Immitzer et al., 2012;
604 Kaszta et al., 2016; Kux and Souza, 2012; Shahi et al., 2017). The comparison of our findings with
605 those coming similar studies carried out in crops (Díaz-Varela et al., 2015; Karydas et al., 2017), but
606 with images acquired by unmanned aerial vehicles (UAVs) and therefore with a higher geometric
607 resolution, gives the idea of the very satisfying results we achieved and the promising potential in
608 reaching the obtained high accuracy applying our methodology to other crops. By the way, according
609 to Wolf (né Straub) and Heipke, 2007, the results on individual tree crown delineation are difficult to
610 standardize and to compare among different researches. This, because of significant differences in
611 study sites, scene characteristics, data sets (spatial and spectral resolutions) and tree types. The shadow

612 effect may probably explain the worst detection rate reported for study area A, coupled with smaller
613 size of olive tree.

614 The effect of shadow has been found to be dependent on the sun azimuth angle in relation to the
615 satellite position at the time of imaging (Leckie et al., 2005) and when this occur vegetation
616 reflectance results disturbed, although satellite over- pass times are programmed to minimize on
617 shadow effect (Chemura et al., 2015). The effect of manual on-screen digitizing of reference data
618 should also be considered when performing the accuracy assessment, and expert knowledge must be
619 provided.

620 The comparison of the spectral reflectance data with the results offered by the pan-sharpened WV-3
621 eight bands orthoimage showed a relatively good agreement between VIs and spectral responses of
622 vegetation and soil targets. Previous studies have already discussed the use of four newly available
623 WV family spectral bands (coastal, green, yellow, red edge) for the classification of the tree species
624 (Immitzer et al., 2012; Pu and Landry, 2012). In our research, it was found that the major differences
625 in spectral behavior, among different plots of the same olive orchard, are mainly due to the component
626 of the red-infrared regions of the EM spectrum, where the RE becomes important in assessing the state
627 of general vigor. It should be pointed out that as we used Digital Numbers (DN) rather than calibrated
628 reflectance values, our results are more qualitative than quantitative, affecting the raw indices results
629 by some modifications in the traditional scale ranges, however ensuring a good description of the
630 vegetation status. As suggested by Candiago et al (2015) VIs were based on DNs due to the absence of
631 ground measurements needed for ground reflectance calibration.

632 VIs results faithfully reflects the different olive orchard vigor conditions among the two-study areas
633 and the different plots. In fact, as confirmed by owners of study area A, over the years, olive orchard
634 have suffered various diseases (olive peacock spot, olive knot disease, olive thrips) that have not
635 allowed an optimal development. Moreover, the soil, mainly clayey and compact, is difficult to work
636 especially in spring and summer seasons, with consequences on plants stress condition. Indeed, a state
637 of better vigor was found in all plots of study area B so that VIs were able to capture the spatial
638 variability of olive tree, deriving from different management practices, such as fertilization or pruning,
639 and the optimal soil condition. Increases in VIs' values in red and NIR bands lead to an increase of

640 canopy cover and LAI, a typical characteristic of green vegetation related to the chlorophyll content
641 and the leaf parenchyma (Horler et al., 1983a; Horler et al., 1983b). VIs based on VIS and NIR
642 reflectance values have been developed taking advantage of the contrast in reflectance behavior
643 between the red and NIR portions of the EM spectrum (Sripada et al., 2008).

644 In this paper, we reported that using reflectance data from WV-3 imagery, could reliably deliver VIs
645 able to detect healthy or unhealthy portions of a cultivated olive orchard. The use of olive tree canopy
646 spectra for vigor assessment mostly depends on the close relationship between nitrogen (N) and
647 chlorophylls in the cell metabolism (Shiratsuchi et al., 2011). The Red band-based VIs like NDVI and
648 NDRE are the most common indices in N status estimation. However, the red band can be easily
649 influenced by soil background reflectance at early growth stages when vegetation coverage is small, as
650 it is in study area A. In our research, the NDRE index significantly improved the estimation results
651 compared to NDVI (Table 6). This is because the RE reflectance is highly correlated with chlorophyll
652 content (Cho and Skidmore, 2006; Clevers et al., 2002), and is responsive to variation in LAI or
653 biomass (Gnyp et al., 2014; Haboudane et al., 2008).

654 In addition, NDRE is insensitive to background effects (Zarco-Tejada et al., 2004). Our results also
655 confirmed the findings of a research on summer maize by Li et al. (2014), who found that the NDRE
656 improved the plant N concentration estimations. The main function of VIs, other than NDVI, also
657 relies on the possibility to compensate for the effects of disturbing factors such as crop type, LAI, or
658 canopy biomass (Bouman, 1995). MCARI2 also succeeded in minimize soil background and LAI
659 variation in olive trees, as found also by (Zarco-Tejada et al., 2004) in providing predictive
660 relationships for chlorophyll concentration estimation with narrow-band imagery in open tree canopy
661 orchards. More in-depth, statistical analysis has shown that the first five bands do not provide
662 additional information under these conditions, reporting no significant difference in all plots and that
663 VIs are mainly influenced by RE, NIR1, and NIR2 values.

664 RE and the two NIR bands explained the most variability, therefore are the main responsible of
665 significant differences in VIs values in the statistical analysis and on which, therefore, depends most
666 of the variability of the vegetative state of the olive trees. This was also observed in wheat LAI
667 estimation by Herrmann et al. (2011). WV-3 band properties, along with indices that are based on

668 reflectance in the RE spectrum region, provided to be very sensitive to olive canopy chlorophyll and
669 N status due to the rapid change in leaf reflectance caused by the strong absorption by pigments in the
670 red spectrum and leaf scattering in the NIR spectrum (Hatfield et al., 2008; Hatfield and Prueger,
671 2010; Nguy-Robertson et al., 2012). This analysis shows the importance of incorporating the RE
672 channel, and two NIR bands particularly in terms of capturing the differences between the decrease
673 and increase in the LAI in an open canopy tree cover. Results show that WV-3 data could improve
674 classification and vegetation health monitoring, coupled with VIs computation, over WV-2 and other
675 satellite sensor as Landsat 8, QuickBird, Pleiades and SPOT (Han et al., 2017; Immitzer et al., 2012;
676 Majid et al., 2016). The additional VNIR bands (including the RE and yellow bands) at fine pixel scale
677 provide a significant improvement over the other satellite platform sensed image. Furthermore, with
678 the additional shortwave infra-red (SWIR) information included in the VW -3 image, the data set
679 could performs as well as a full hyperspectral sensor (Han et al., 2017).

680 This study demonstrated that high spatial resolution satellite data makes olive orchard precision
681 monitoring possible, and in further studies, radiometric ground truth data can be used to calibrate and
682 map the time series of olive growth condition, filling the limits of this method, applied to relatively
683 large, homogeneous, single-layer agricultural or forest ecosystems (Maselli et al. 2014). To address
684 PA applications to spatially fragmented and multi-layer agricultural ecosystems that are common in
685 southern Mediterranean rural areas, there is the need to face with further challenges. One of the most
686 important concerns the spatial distribution and size of most of the European agricultural olive groves
687 systems, as well as vineyards an any tree plantations, which are generally far below the resolution of
688 widely used remote sensed imagery (Landsat or MODIS). These ecosystems are found over irregular
689 terrain and occupy small unit areas (around 0.1–0.5 ha) (Maselli et al., 2012) in many agricultural
690 situations. Among the possible solutions implemented by research, one of the most common solutions
691 that are being adopted could be the integration of high spatial resolution satellite data, such as WV-3
692 data, with those acquired through UAVs with higher spatial resolution. This is confirmed by recent
693 experimental studies carried out in several crop systems (Palchowdhuri et al., 2018), which indicate
694 that such integration leads to a clear improvement in crop management. The VW series of satellites
695 (2009) provided further enhancements to spectral monitoring with 8 multi-spectral bands at very high

696 spatial resolutions in addition to 8 SWIR bands. Despite sensor capabilities, the potential of WV-3
697 imagery for PA purposes has yet to be fully realized due to prohibitively expensive image acquisition
698 costs, even in the context of continuous monitoring. This highlights the gap currently existing between
699 expensive commercial and free data systems in terms of their potential applications, particularly
700 evident in the case of PA (Houborg et al., 2015). To this end the pair of new Sentinel-2 satellites (S-
701 2A, S-2B), will bridge this gap by delivering narrower band multispectral data (including 2 narrow
702 bands in RE) at 10 m resolutions with a 5 days revisit frequency. Despite of a spatial resolution lower
703 than WV-3, this will give the opportunity to significantly improve the ability to monitor the state and
704 function of worldwide vegetation, through enhanced definition of the RE coupled with crop scouting.
705 Therefore, agricultural systems could be monitored throughout the growing season and a reliable
706 decision support system, based on RS information, could be achievable (Basso et al., 2004; Wojtowicz
707 et al., 2016).

708

709 **6. Conclusions**

710 The present paper showed the main findings and the potentialities of a semiautomatic process
711 workflow implemented on WV-3 imagery and aimed at obtaining VIs at tree detail in olive crops,
712 without any ground radiometric measure. The results from this study confirm the potential of high
713 resolution WV-3 imagery for accurately derive olive tree crown boundaries across two different olive
714 orchards in Calabria region, southern Italy. Tree crown detection and extraction were optimized, thus
715 achieving high geometric accuracy obtaining a close to real canopy shape boundary.

716 VIs maps revealed more contrast and more properties than those resulting visually evident from true
717 and false colors image analysis, while the spatial distribution of NDVI, MSAVI2, NDRE, MCARI2,
718 NDVI2 already showed significant pattern, where the zones with negative behavior were well
719 recognizable. Due to the heterogeneous extension and composition characterizing agricultural
720 ecosystems in southern Mediterranean areas, visual interpretation and tree detection can be
721 significantly improved by the data enrichment provided through the sharpening of WV-3 multispectral
722 bands with the panchromatic one.

723 Statistical analyses showed that the major differences in spectral behavior, over different plots of the
724 two investigated olive orchards, are mainly due to the component of the red-infrared regions of the
725 EM spectrum, where the RE becomes important in assessing the state of vegetation vigor.
726 The proposed classification method is very promising, since it provides an operational processing
727 chain for mapping and monitoring olive orchards at tree detail, thus allowing to identify healthy or
728 unhealthy portions of the analyzed crop. On the other hand, our study confirms that GEOBIA
729 classification and single tree crown extraction benefit from suitable conditions of olive crops
730 characterized by regular planting patterns with minimum overlap. Additional RS technologies, such as
731 a low-altitude remote sensing based on UAVs, may be adopted to overcome these limitations. By the
732 way, satellite imagery has proven to be cost-effective compared to UAV imagery in terms of area
733 coverage, processing and pre-processing need for geometric and radiometric calibrations, spectral
734 information, and less costs in collecting reference data sampling.

735 This study provided a novel contribution in exploring the reliability of WV-3 multispectral imagery in
736 PA applications. The proposed methodology, when applied to an operational field, has proven to be
737 quick and cost-effective. Moreover, our research offers an original and innovative contribution
738 increasing the knowledge in olive crop management and monitoring, at tree detail, from VHR satellite
739 imagery.

740 At the present stage of our research, our findings and conclusions could be extended to other cases
741 only after comparison with the results of other studies concerning olive orchard conditions similar to
742 those here investigated. Further studies may investigate how to take advantage from high spatial
743 resolution satellite imagery, as that provided by WV-3 sensor, by linking it to an adequate ground truth
744 data collection.

745

746 **Acknowledgements** This research has been funded by projects PONa3_00016-RI-SAF@MED (Research
747 Infrastructure for Sustainable Agriculture and Food in Mediterranean area) and PON03PE_00090_2, in the
748 framework of National Operational Program (NOP) for Research and Competitiveness 2007-2013 of the Italian
749 Ministry of Education, University and Research (MIUR) and Ministry of Economic Development (MiSE), and
750 co-funded by the European Regional Development Fund (ERDF).

751

752 **7. References**

- 753 Aguilar, M. a, Saldaña, M.M., Aguilar, F.J., 2013. GeoEye-1 and WorldView-2 pan- sharpened imagery for
754 object-based classification in urban environments. *Int. J. Remote Sens.* 34, 2583–2606.
755 doi:10.1080/01431161.2012.747018
- 756 Aguilar, M.A., Aguilar, F.J., García Lorca, A., Guirado, E., Betlej, M., Cichon, P., Nemmaoui, A., Vallario, A.,
757 Parente, C., 2016. Assessment of multiresolution segmentation for extracting greenhouses from
758 WorldView-2 imagery. *Int. Arch. Photogramm. Remote Sens. Spat. Inf. Sci. - ISPRS Arch.* 41, 145–152.
759 doi:10.5194/isprsarchives-XLI-B7-145-2016
- 760 Alrassi, F., Salim, E., Nina, A., Alwi, L., Danoedoro, P., Kamal, M., 2016. GEOBIA for Land Use Mapping
761 Using Worldview2 Image in Bengkak Village Coastal, Banyuwangi Regency, East Java. *IOP Conf. Ser.*
762 *Earth Environ. Sci.* 47. doi:10.1088/1755-1315/47/1/012009
- 763 Anderson, N.T., Underwood, J.P., Rahman, M.M., Robson, A., Walsh, K.B., 2018. Estimation of fruit load in
764 mango orchards: tree sampling considerations and use of machine vision and satellite imagery. *Precis.*
765 *Agric.* 1–17. doi:10.1007/s11119-018-9614-1
- 766 Balthazar, V., Vanacker, V., Lambin, E.F., 2012. Evaluation and parameterization of ATCOR3 topographic
767 correction method for forest cover mapping in mountain areas. *Int. J. Appl. Earth Obs. Geoinf.* 18, 436–
768 450. doi:10.1016/j.jag.2012.03.010
- 769 Barnes, E., Clarke, T., Richards, S., Colaizzi, P., Haberland, J., Kostrzewski, M., Waller, P., Choi, C., Riley, E.,
770 Thompson, T., Lascano, R.J., Li, H., Moran, M., 2000. Coincident detection of crop water stress, nitrogen
771 status and canopy density using ground-based multispectral data, in: *Fifth International Conference on*
772 *Precision Agriculture.*
- 773 Basso, B., Cammarano, D., De Vita, P., 2004. Remotely sensed vegetation indices: Theory and applications for
774 crop management. *Ital. J. Agrometeorol.* 53, 36–53.
- 775 Bausch, W.C., Khosla, R., 2010. QuickBird satellite versus ground-based multi-spectral data for estimating
776 nitrogen status of irrigated maize. *Precis. Agric.* 11, 274–290. doi:10.1007/s11119-009-9133-1
- 777 Benalia, S., Bernardi, B., Blasco, J., Fazari, A., Zimbalatti, G., 2017. Assessment of the Ripening of Olives
778 Using Computer Vision. *Chem. Eng. Trans.* 58, 355–360. doi:10.3303/CET1758060
- 779 Blaschke, T., 2010. Object based image analysis for remote sensing. *ISPRS J. Photogramm. Remote Sens.* 65, 2–
780 16. doi:10.1016/j.isprsjprs.2009.06.004
- 781 Blaschke, T., Hay, G.J., Kelly, M., Lang, S., Hofmann, P., Addink, E., Queiroz Feitosa, R., van der Meer, F., van
782 der Werff, H., van Coillie, F., Tiede, D., 2014. Geographic Object-Based Image Analysis – Towards a new
783 paradigm. *ISPRS J. Photogramm. Remote Sens.* 87, 180–191. doi:10.1016/j.isprsjprs.2013.09.014
- 784 Bouman, B.A.M., 1995. Crop modelling and remote sensing for yield prediction. *Netherl. J. Agric. Sci.* 43, 143–
785 161.
- 786 Broge, N.H., Leblanc, E., 2001. Comparing prediction power and stability of broadband and hyperspectral
787 vegetation indices for estimation of green leaf area index and canopy chlorophyll density. *Remote Sens.*
788 *Environ.* 76, 156–172. doi:10.1016/S0034-4257(00)00197-8
- 789 Calderón, R., Navas-Cortés, J.A., Lucena, C., Zarco-Tejada, P.J., 2013. High-resolution airborne hyperspectral
790 and thermal imagery for early detection of Verticillium wilt of olive using fluorescence, temperature and
791 narrow-band spectral indices. *Remote Sens. Environ.* 139, 231–245. doi:10.1016/j.rse.2013.07.031
- 792 Calderón, R., Navas-Cortés, J.A., Zarco-Tejada, P.J., 2015. Early detection and quantification of Verticillium
793 Wilt in olive using hyperspectral and thermal imagery over large areas. *Remote Sens.* 7, 5584–5610.
794 doi:10.3390/rs70505584
- 795 Calvão, T., Palmeirim, J.M., 2004. Mapping Mediterranean scrub with satellite imagery: biomass estimation and
796 spectral behaviour. *Int. J. Remote Sens.* 25, 3113–3126. doi:10.1080/01431160310001654978
- 797 Cammarano, D., Fitzgerald, G.J., Casa, R., Basso, B., 2014. Assessing the robustness of vegetation indices to
798 estimate wheat N in mediterranean environments. *Remote Sens.* 6, 2827–2844. doi:10.3390/rs6042827
- 799 Chemura, A., van Duren, I., van Leeuwen, L.M., 2015. Determination of the age of oil palm from crown
800 projection area detected from WorldView-2 multispectral remote sensing data: The case of Ejisu-Juaben
801 district, Ghana. *ISPRS J. Photogramm. Remote Sens.* 100, 118–127. doi:10.1016/j.isprsjprs.2014.07.013
- 802 Chepkochei, L., 2011. Object-oriented image classification of individual trees using Erdas Imagine Objective:
803 Case study of Wanjohi area, Lake Naivasha Basin, Kenya. *Proceedings, Kenya Geotherm. Conf.*

- 804 Cho, M.A., Skidmore, A.K., 2006. A new technique for extracting the red edge position from hyperspectral data:
805 The linear extrapolation method. *Remote Sens. Environ.* 101, 181–193. doi:10.1016/j.rse.2005.12.011
- 806 Chuang, Y.C.M., Shiu, Y.S., 2016. A comparative analysis of machine learning with worldview-2 pan-
807 sharpened imagery for tea crop mapping. *Sensors (Switzerland)* 16. doi:10.3390/s16050594
- 808 Clevers, J.G.P.W., De Jong, S.M., Epema, G.F., Van Der Meer, F.D., Bakker, W.H., Skidmore, A.K., Scholte,
809 K.H., 2002. Derivation of the red edge index using the MERIS standard band setting. *Int. J. Remote Sens.*
810 23, 3169–3184. doi:10.1080/01431160110104647
- 811 Congalton, R.G., 1991. A review of assessing the accuracy of classifications of remotely sensed data. *Remote*
812 *Sens. Environ.* 37, 35–46. doi:10.1016/0034-4257(91)90048-B
- 813 Congalton, R.G., Green, K., 2008. *Assessing the Accuracy of Remotely Sensed Data: Principles and Practices,*
814 *Second Edition, Second Edi. ed. CRC Press.*
- 815 Dahiya, S., Garg, P.K., Jat, M.K., 2013. A comparative study of various pixel-based image fusion techniques as
816 applied to an urban environment. *Int. J. Image Data Fusion* 4, 197–213.
817 doi:10.1080/19479832.2013.778335
- 818 Daughtry, C., 2000. Estimating Corn Leaf Chlorophyll Concentration from Leaf and Canopy Reflectance.
819 *Remote Sens. Environ.* 74, 229–239. doi:10.1016/S0034-4257(00)00113-9
- 820 de Graaff, J., Eppink, L.A.A., 1999. Olive oil production and soil conservation in southern Spain, in relation to
821 EU subsidy policies. *Land use policy* 16, 259–267. doi:10.1016/S0264-8377(99)00022-8
- 822 Di Fazio, S., Modica, G., 2018. Historic Rural Landscapes: Sustainable Planning Strategies and Action Criteria.
823 The Italian Experience in the Global and European Context. *Sustainability* 10, 3834.
824 doi:10.3390/su10113834
- 825 Díaz-Varela, R., de la Rosa, R., León, L., Zarco-Tejada, P., 2015. High-Resolution Airborne UAV Imagery to
826 Assess Olive Tree Crown Parameters Using 3D Photo Reconstruction: Application in Breeding Trials.
827 *Remote Sens.* 7, 4213–4232. doi:10.3390/rs70404213
- 828 Eckert, S., 2012. Improved Forest Biomass and Carbon Estimations Using Texture Measures from WorldView-2
829 Satellite Data. *Remote Sens.* 4, 810–829. doi:10.3390/rs4040810
- 830 Eitel, J.U.H., Long, D.S., Gessler, P.E., Smith, A.M.S., 2007. Using in-situ measurements to evaluate the new
831 RapidEye™ satellite series for prediction of wheat nitrogen status. *Int. J. Remote Sens.* 28, 4183–4190.
832 doi:10.1080/01431160701422213
- 833 Erikson, M., 2004. Species classification of individually segmented tree crowns in high-resolution aerial images
834 using radiometric and morphologic image measures. *Remote Sens. Environ.* 91, 469–477.
835 doi:10.1016/j.rse.2004.04.006
- 836 Fitzgerald, G.J., 2010. Characterizing vegetation indices derived from active and passive sensors. *Int. J. Remote*
837 *Sens.* 31, 4335–4348. doi:10.1080/01431160903258217
- 838 Foxhall, L., 2007. *Olive Cultivation in Ancient Greece: Seeking the Ancient Economy.* Oxford University Press,
839 New York, NY, USA.
- 840 Gaertner, J., 2017. Vegetation classification of Coffea on Hawaii Island using WorldView-2 satellite imagery. *J.*
841 *Appl. Remote Sens.* 11, 1. doi:10.1117/1.JRS.11.046005
- 842 Gnyp, M.L., Miao, Y., Yuan, F., Ustin, S.L., Yu, K., Yao, Y., Huang, S., Bareth, G., 2014. Hyperspectral canopy
843 sensing of paddy rice aboveground biomass at different growth stages. *F. Crop. Res.* 155, 42–55.
844 doi:10.1016/j.fcr.2013.09.023
- 845 Goutte, C., Gaussier, E., 2005. A Probabilistic Interpretation of Precision, Recall and F-Score, with Implication
846 for Evaluation. pp. 345–359. doi:10.1007/978-3-540-31865-1_25
- 847 Haboudane, D., Miller, J.R., Pattey, E., Zarco-Tejada, P.J., Strachan, I.B., 2004. Hyperspectral vegetation
848 indices and novel algorithms for predicting green LAI of crop canopies: Modeling and validation in the
849 context of precision agriculture. *Remote Sens. Environ.* 90, 337–352. doi:10.1016/j.rse.2003.12.013
- 850 Haboudane, D., Tremblay, N., Miller, J.R., Vigneault, P., 2008. Remote Estimation of Crop Chlorophyll Content
851 Using Spectral Indices Derived From Hyperspectral Data. *IEEE Trans. Geosci. Remote Sens.* 46, 423–437.
852 doi:10.1109/TGRS.2007.904836
- 853 Han, J., Wei, C., Chen, Y., Liu, W., Song, P., Zhang, D., Wang, A., Song, X., Wang, X., Huang, J., 2017.

- 854 Mapping Above-Ground Biomass of Winter Oilseed Rape Using High Spatial Resolution Satellite Data at
855 Parcel Scale under Waterlogging Conditions. *Remote Sens.* 9, 238. doi:10.3390/rs9030238
- 856 Hatfield, J.L., Gitelson, A.A., Schepers, J., Walthall, C.L., 2008. Application of Spectral Remote Sensing for
857 Agronomic Decisions. *Agron. J.* S-117-S-131. doi:10.2134/agronj2006.0370c
- 858 Hatfield, J.L., Prueger, J.H., 2010. Value of Using Different Vegetative Indices to Quantify Agricultural Crop
859 Characteristics at Different Growth Stages under Varying Management Practices. *Remote Sens.* 2, 562–
860 578. doi:10.3390/rs2020562
- 861 Herrmann, I., Pimstein, A., Carnieli, A., Cohen, Y., Alchanatis, V., Bonfil, D.J., 2011. LAI assessment of wheat
862 and potato crops by VEN μ S and Sentinel-2 bands. *Remote Sens. Environ.* 115, 2141–2151.
863 doi:10.1016/j.rse.2011.04.018
- 864 Horler, D. N. H., Dockray, M., Barber, J., 1983. The red edge of plant leaf reflectance. *Int. J. Remote Sens.* 4,
865 273–288. doi:10.1080/01431168308948546
- 866 Horler, D.N.H., Dockray, M., Barber, J., Barringer, A.R., 1983. Red edge measurements for remotely sensing
867 plant chlorophyll content. *Adv. Sp. Res.* 3, 273–277. doi:10.1016/0273-1177(83)90130-8
- 868 Houborg, R., McCabe, M., Cescatti, A., Gao, F., Schull, M., Gitelson, A., 2015. Joint leaf chlorophyll content
869 and leaf area index retrieval from Landsat data using a regularized model inversion system (REGFLEC).
870 *Remote Sens. Environ.* 159, 203–221. doi:10.1016/j.rse.2014.12.008
- 871 Huete, A.R., 1988. A Soil-Adjusted Vegetation Index (SAVI). *Remote Sens. Environ.* 309, 295–309.
872 doi:10.1016/0034-4257(88)90106-X
- 873 Hunt, E.R., Doraiswamy, P.C., McMurtrey, J.E., Daughtry, C.S.T., Perry, E.M., Akhmedov, B., 2013. A visible
874 band index for remote sensing leaf chlorophyll content at the canopy scale. *Int. J. Appl. Earth Obs. Geoinf.*
875 21, 103–112. doi:10.1016/j.jag.2012.07.020
- 876 Hunt, E.R., Doraiswamy, P.C., McMurtrey, J.E., Daughtry, C.S.T., Perry, E.M., Akhmedov, B., 2012. A visible
877 band index for remote sensing leaf chlorophyll content at the Canopy scale. *Int. J. Appl. Earth Obs.*
878 *Geoinf.* 21, 103–112. doi:10.1016/j.jag.2012.07.020
- 879 Immitzer, M., Atzberger, C., Koukal, T., 2012. Tree Species Classification with Random Forest Using Very
880 High Spatial Resolution 8-Band WorldView-2 Satellite Data. *Remote Sens.* 4, 2661–2693.
881 doi:10.3390/rs4092661
- 882 International Olive Council, 2018. World Olive Oil Figures [WWW Document]. URL
883 <http://www.internationaloliveoil.org/estaticos/view/131-world-olive-oil-figures> (accessed 10.30.18).
- 884 ISMEA, 2018. Piano di settore Olivicolo-oleario. La produzione italiana di olio di oliva. Stime della campagna
885 produttiva 2017/18. Rome, Italy.
- 886 Johnson, K.E., Staff, R., Scientist, D., 2017. WorldView-3 Swir land use-land cover mineral classification:
887 Cuprite, NEVADA, in: *Observing a Changing Earth; Science for Decisions— Monitoring, Assessment,*
888 *and Projection.* Sioux Falls, SD.
- 889 Jolliffe, I.T., 2002. *Principal Component Analysis.* Second Edition. Springer Ser. Stat. 98, 487.
890 doi:10.1007/b98835
- 891 Karydas, C., Gewehr, S., Iatrou, M., Iatrou, G., Mourelatos, S., 2017. Olive Plantation Mapping on a Sub-Tree
892 Scale with Object-Based Image Analysis of Multispectral UAV Data; Operational Potential in Tree Stress
893 Monitoring. *J. Imaging* 3, 57. doi:10.3390/jimaging3040057
- 894 Kaszta, Z., Van De Kerchove, R., Ramoelo, A., Cho, M.A., Madonsela, S., Mathieu, R., Wolff, E., 2016.
895 Seasonal separation of African savanna components using WorldView-2 imagery: A comparison of
896 pixeland object-based approaches and selected classification algorithms. *Remote Sens.* 8.
897 doi:10.3390/rs8090763
- 898 Koc-San, D., Selim, S., Aslan, N., San, B.T., 2018. Automatic citrus tree extraction from UAV images and
899 digital surface models using circular Hough transform. *Comput. Electron. Agric.* 150, 289–301.
900 doi:10.1016/j.compag.2018.05.001
- 901 Koenig, J., Gueguen, L., 2016. A comparison of land use land cover classification using superspectral
902 WorldView-3 vs hyperspectral imagery, in: *2016 8th Workshop on Hyperspectral Image and Signal*
903 *Processing: Evolution in Remote Sensing (WHISPERS).* IEEE, pp. 1–5.
904 doi:10.1109/WHISPERS.2016.8071721

- 905 Kumar, M., Monteith, J.L., 1981. Remote sensing of crop growth, in: Smith, H. (Ed.), *Plants and the Daylight*
906 *Spectrum*. Academic Press, London, pp. 133–144.
- 907 Kux, H.J.H., Souza, U.D. V., 2012. Object-Based Image Analysis of Worldview-2 Satellite Data for the
908 Classification of Mangrove Areas in the City of São Luís, Maranhão State, Brazil. *ISPRS Ann.*
909 *Photogramm. Remote Sens. Spat. Inf. Sci.* 1–4, 95–100. doi:10.5194/isprsannals-I-4-95-2012
- 910 Larsen, M., Eriksson, M., Descombes, X., Perrin, G., Brandtberg, T., Gougeon, F.A., 2011. Comparison of six
911 individual tree crown detection algorithms evaluated under varying forest conditions. *Int. J. Remote Sens.*
912 32, 5827–5852. doi:10.1080/01431161.2010.507790
- 913 Leckie, D.G., Gougeon, F.A., Tinis, S., Nelson, T., Burnett, C.N., Paradine, D., 2005. Automated tree
914 recognition in old growth conifer stands with high resolution digital imagery. *Remote Sens. Environ.* 94,
915 311–326. doi:10.1016/j.rse.2004.10.011
- 916 Li, F., Miao, Y., Feng, G., Yuan, F., Yue, S., Gao, X., Liu, Y., Liu, B., Ustin, S.L., Chen, X., 2014. Improving
917 estimation of summer maize nitrogen status with red edge-based spectral vegetation indices. *F. Crop. Res.*
918 157, 111–123. doi:10.1016/j.fcr.2013.12.018
- 919 Li, W., Guo, Q., Jakubowski, M.K., Kelly, M., 2012. A New Method for Segmenting Individual Trees from the
920 Lidar Point Cloud. *Photogramm. Eng. Remote Sens.* 78, 75–84. doi:10.14358/PERS.78.1.75
- 921 Loumou, A., Giourga, C., 2003. Olive groves: “The life and identity of the Mediterranean”.” *Agric. Human*
922 *Values* 20, 87–95. doi:10.1023/A:1022444005336
- 923 Lu, X., Guo, Q., Li, W., Flanagan, J., 2014. A bottom-up approach to segment individual deciduous trees using
924 leaf-off lidar point cloud data. *ISPRS J. Photogramm. Remote Sens.* 94, 1–12.
925 doi:10.1016/j.isprsjprs.2014.03.014
- 926 Main, R., Cho, M.A., Mathieu, R., O’Kennedy, M.M., Ramoelo, A., Koch, S., 2011. An investigation into robust
927 spectral indices for leaf chlorophyll estimation. *ISPRS J. Photogramm. Remote Sens.* 66, 751–761.
928 doi:10.1016/j.isprsjprs.2011.08.001
- 929 Majid, I.A., Latif, Z.A., Adnan, N.A., 2016. Tree Species Classification Using Worldview-3 Data.
- 930 Maselli, F., Chiesi, M., Brilli, L., Moriondo, M., 2012. Simulation of olive fruit yield in Tuscany through the
931 integration of remote sensing and ground data. *Ecol. Modell.* 244, 1–12.
932 doi:10.1016/j.ecolmodel.2012.06.028
- 933 Maselli, F., Papale, D., Chiesi, M., Matteucci, G., Angeli, L., Raschi, A., Seufert, G., 2014. Operational
934 monitoring of daily evapotranspiration by the combination of MODIS NDVI and ground meteorological
935 data: Application and evaluation in Central Italy. *Remote Sens. Environ.* 152, 279–290.
936 doi:10.1016/j.rse.2014.06.021
- 937 Moder, K., 2010. Alternatives to F-Test in One Way ANOVA in case of heterogeneity of variances (a simulation
938 study). *Psychol. Test Assess. Model.* 52, 343–353.
- 939 Modica, G., Pollino, M., Solano, F., 2019. Sentinel-2 Imagery for Mapping Cork Oak (*Quercus suber* L.)
940 Distribution in Calabria (Italy): Capabilities and Quantitative Estimation, in: Calabrò, F., Della Spina, L.,
941 Bevilacqua, C. (Eds.), *New Metropolitan Perspectives. ISHT 2018. Smart Innovation, Systems and*
942 *Technologies*. Springer, Cham, pp. 60–67. doi:10.1007/978-3-319-92099-3_8
- 943 Mutanga, O., Adam, E., Adjorlolo, C., Abdel-Rahman, E.M., 2015. Evaluating the robustness of models
944 developed from field spectral data in predicting African grass foliar nitrogen concentration using
945 WorldView-2 image as an independent test dataset. *Int. J. Appl. Earth Obs. Geoinf.* 34, 178–187.
946 doi:10.1016/j.jag.2014.08.008
- 947 Nebikera, S., Nebikera, S., Annena, A., Scherrerb, M., Oeschc, D., 2008. A Light-weight Multispectral Sensor
948 for Micro UAV - Opportunities for very high resolution airborne remote sensing. *Int. Arch. Photogramm.*
949 *Remote Sens. Spat. Inf. Sci.* 1193–1200.
- 950 Ng, W.-T., Rima, P., Einzmann, K., Immitzer, M., Atzberger, C., Eckert, S., 2017. Assessing the Potential of
951 Sentinel-2 and Pléiades Data for the Detection of *Prosopis* and *Vachellia* spp. in Kenya. *Remote Sens.* 9,
952 74. doi:10.3390/rs9010074
- 953 Nguy-Robertson, A., Gitelson, A., Peng, Y., Vina, A., Arkebauer, T., Rundquist, D., 2012. Green leaf area index
954 estimation in maize and soybean: combining vegetation indices to achieve maximal sensitivity. *Agron. J.*
955 1336–1347. doi:10.2134/agronj2012.0065

- 956 Ok, A.O., Senaras, C., Yuksel, B., 2013. Automated detection of arbitrarily shaped buildings in complex
957 environments from monocular VHR optical satellite imagery. *IEEE Trans. Geosci. Remote Sens.* 51,
958 1701–1717. doi:10.1109/TGRS.2012.2207123
- 959 Ortega-Farías, S., Ortega-Salazar, S., Poblete, T., Kilic, A., Allen, R., Poblete-Echeverría, C., Ahumada-
960 Orellana, L., Zuñiga, M., Sepúlveda, D., 2016. Estimation of Energy Balance Components over a Drip-
961 Irrigated Olive Orchard Using Thermal and Multispectral Cameras Placed on a Helicopter-Based
962 Unmanned Aerial Vehicle (UAV). *Remote Sens.* 8, 638. doi:10.3390/rs8080638
- 963 Padwick, C., Deskevich, M., Pacifici, F., Smallwood, S., 2010. Worldview-2 pan-sharpening, in: ASPRS 2010
964 Annual Conference. San Diego, California.
- 965 Palchowdhuri, Y., Valcarce-Diñeiro, R., King, P., Sanabria-Soto, M., 2018. Classification of multi-temporal
966 spectral indices for crop type mapping: A case study in Coalville, UK. *J. Agric. Sci.* 156, 24–36.
967 doi:10.1017/S0021859617000879
- 968 Pauly, K., 2014. Applying Conventional Vegetation Vigor Indices To UAS-Derived Orthomosaics: Issues And
969 Considerations. Ispa.
- 970 Petrucci, O., Polemio, M., Pasqua, A.A., 2009. Analysis of damaging hydrogeological events: The case of the
971 Calabria region (Southern Italy). *Environ. Manage.* 43, 483–495. doi:10.1007/s00267-008-9234-z
- 972 Pettorelli, N., 2013. *The Normalized Difference Vegetation Index*. Oxford University Press, Oxford, UK.
- 973 Prince, S.D., 1990. High temporal frequency remote sensing of primary production using NOAA AVHRR, in:
974 Applications of Remote Sensing in Agriculture. Elsevier, pp. 169–183. doi:10.1016/B978-0-408-04767-
975 8.50016-5
- 976 Pu, R., Landry, S., 2012. A comparative analysis of high spatial resolution IKONOS and WorldView-2 imagery
977 for mapping urban tree species. *Remote Sens. Environ.* 124, 516–533. doi:10.1016/j.rse.2012.06.011
- 978 Qi, J., Chehbouni, A., Huete, A.R., Kerr, Y.H., Sorooshian, S., 1994. A modified soil adjusted vegetation index.
979 *Remote Sens. Environ.* 48, 119–126. doi:10.1016/0034-4257(94)90134-1
- 980 R Core Team, 2017. *R: A language and environment for statistical computing*.
- 981 Rahman, M., Robson, A., Bristow, M., Rahman, M.M., Robson, A., Bristow, M., 2018. Exploring the Potential
982 of High Resolution WorldView-3 Imagery for Estimating Yield of Mango. *Remote Sens.* 10, 1866.
983 doi:10.3390/rs10121866
- 984 Richards, J.A., Jia, X., 2006. *Remote Sensing Digital Image Analysis. An introduction*. Springer-Verlag,
985 Berlin/Heidelberg. doi:10.1007/3-540-29711-1
- 986 Richter, R., 1998. Correction of satellite imagery over mountainous terrain. *Appl. Opt.* 37, 4004–15.
- 987 Richter, R., 1997. Correction of atmospheric and topographic effects for high spatial resolution satellite imagery.
988 *Int. J. Remote Sens.* 18, 1099–1111. doi:10.1080/014311697218593
- 989 Richter, R., Kellenberger, T., Kaufmann, H., 2009. Comparison of Topographic Correction Methods. *Remote
990 Sens.* 1, 184–196. doi:10.3390/rs1030184
- 991 Roberts, D., Roth, K., Perroy, R., 2011. Hyperspectral Vegetation Indices, in: *Hyperspectral Remote Sensing of
992 Vegetation*. CRC Press, pp. 309–328. doi:10.1201/b11222-20
- 993 Robson, A., Rahman, M., Muir, J., Robson, A., Rahman, M.M., Muir, J., 2017. Using Worldview Satellite
994 Imagery to Map Yield in Avocado (*Persea americana*): A Case Study in Bundaberg, Australia. *Remote
995 Sens.* 9, 1223. doi:10.3390/rs9121223
- 996 Rouse, J.W., Haas, R.H., Schell, J.A., Deering, D.W., 1974. Monitoring Vegetation Systems in the Great Plains
997 with Erts, in: Stanley Freden, C., Mercanti, Enrico P., Becker, M.A. (Eds.), *Third Earth Resources
998 Technology Satellite 1 Symposium*. NASA, Washington, D.C., USA.
- 999 Sepulcre-Cantò, G., Zarco-Tejada, P.J., Sobrino, J. a., Jimenez-Munoz, J.C., Villalobos, E., 2005. Spatial
1000 variability of crop water stress in an olive grove with high-spatial thermal remote sensing imagery. *Precis.
1001 Agric.* '05 267–272.
- 1002 Shahi, K., Shafri, H.Z.M., Hamedianfar, A., 2017. Road condition assessment by OBIA and feature selection
1003 techniques using very high-resolution WorldView-2 imagery. *Geocarto Int.* 32, 1389–1406.
1004 doi:10.1080/10106049.2016.1213888

- 1005 Shiratsuchi, L., Ferguson, R., Shanahan, J., Adamchuk, V., Rundquist, D., Marx, D., Slater, G., 2011. Water and
 1006 Nitrogen Effects on Active Canopy Sensor Vegetation Indices. *Agron. J.* 103, 1815.
 1007 doi:10.2134/agronj2011.0199
- 1008 Shojanoori, R., Shafri, H.Z.M., Mansor, S., Ismail, M.H., 2016. The Use of WorldView-2 Satellite Data in
 1009 Urban Tree Species Mapping by Object-Based Image Analysis Technique. *Sains Malaysiana* 45, 1025–
 1010 1034.
- 1011 Siegmann, B., Jarmer, T., Lilienthal, H., Richter, N., Selige, T., Sensing, R., 2012. Comparison of Narrow Band
 1012 Vegetation Indices and Empirical Models From Hyperspectral Remote Sensing Data for the Assessment of
 1013 Wheat Nitrogen Concentration.
- 1014 Sokolova, M., Japkowicz, N., Szpakowicz, S., 2006. Beyond Accuracy, F-Score and ROC: A Family of
 1015 Discriminant Measures for Performance Evaluation 1015–1021. doi:10.1007/11941439_114
- 1016 Srestasathiern, P., Rakwatin, P., 2014. Oil Palm Tree Detection with High Resolution Multi-Spectral Satellite
 1017 Imagery. *Remote Sens.* 6, 9749–9774. doi:10.3390/rs6109749
- 1018 Sripada, R.P., Schmidt, J.P., Dellinger, A.E., Beegle, D.B., 2008. Evaluating Multiple Indices from a Canopy
 1019 Reflectance Sensor to Estimate Corn N Requirements. *Agron. J.* 100, 1553. doi:10.2134/agronj2008.0017
- 1020 Tardi, A., 2014. The culinary uses of extra-virgin olive oil, in: Peri, C. (Ed.), *The Extra-Virgin Olive Oil*
 1021 *Handbook*. Wiley-Blackwell, Oxford, UK, p. 380.
- 1022 Tucker, C.J., 1979. Red and photographic infrared linear combinations for monitoring vegetation. *Remote Sens.*
 1023 *Environ.* 8, 127–150. doi:10.1016/0034-4257(79)90013-0
- 1024 Vanonckelen, S., Lhermitte, S., Balthazar, V., Van Rompaey, A., 2014. Performance of atmospheric and
 1025 topographic correction methods on Landsat imagery in mountain areas. *Int. J. Remote Sens.* 35, 4952–
 1026 4972. doi:10.1080/01431161.2014.933280
- 1027 Veroustraete, F., Sabbe, H., Eerens, H., 2002. Estimation of carbon mass fluxes over Europe using the C-Fix
 1028 model and Euroflux data. *Remote Sens. Environ.* 83, 376–399. doi:10.1016/S0034-4257(02)00043-3
- 1029 Villalobos, F.J., Testi, L., Hidalgo, J., Pastor, M., Orgaz, F., 2006. Modelling potential growth and yield of olive
 1030 (*Olea europaea* L.) canopies. *Eur. J. Agron.* 24, 296–303. doi:10.1016/j.eja.2005.10.008
- 1031 Vincini, M., Frazzi, E., D'Alessio, P., 2008. A broad-band leaf chlorophyll vegetation index at the canopy scale.
 1032 *Precis. Agric.* 9, 303–319. doi:10.1007/s11119-008-9075-z
- 1033 Vossen, P., 2007. Olive Oil: History, Production, and Characteristics of the World's Classic Oils. *HortScience*
 1034 42, 1093–1100.
- 1035 Wallace, J.F., Caccetta, P.A., Kiiveri, H.T., 2004. Recent developments in analysis of spatial and temporal data
 1036 for landscape qualities and monitoring. *Austral Ecol.* 29, 100–107. doi:10.1111/j.1442-9993.2004.01356.x
- 1037 Wang, L., Gong, P., Biging, G.S., 2004. Individual Tree-Crown Delineation and Treetop Detection in High-
 1038 Spatial-Resolution Aerial Imagery. *Photogramm. Eng. Remote Sens.* 70, 351–357.
 1039 doi:10.14358/PERS.70.3.351
- 1040 Waser, L.T., Küchler, M., Jütte, K., Stampfer, T., 2014. Evaluating the potential of worldview-2 data to classify
 1041 tree species and different levels of ash mortality. *Remote Sens.* 6, 4515–4545. doi:10.3390/rs6054515
- 1042 Wojtowicz, M., Wojtowicz, A., Piekarczyk, J., 2016. Application of remote sensing methods in agriculture.
 1043 *Commun. Biometry Crop Sci.* 11, 31–50.
- 1044 Wolf (né Straub), B.-M., Heipke, C., 2007. Automatic extraction and delineation of single trees from remote
 1045 sensing data. *Mach. Vis. Appl.* 18, 317–330. doi:10.1007/s00138-006-0064-9
- 1046 Wolf, A.F., 2012. Using WorldView-2 Vis-NIR multispectral imagery to support land mapping and feature
 1047 extraction using normalized difference index ratios. *Proc. SPIE* 8390, 83900N-83900N–8.
 1048 doi:10.1117/12.917717
- 1049 Ye, B., Tian, S., Ge, J., Sun, Y., 2017. Assessment of WorldView-3 data for lithological mapping. *Remote Sens.*
 1050 9, 1–19. doi:10.3390/rs9111132
- 1051 Zar, J.H., 1996. *Biostatistical analysis*, 3rd editio. ed. Prentice Hall International, London.
- 1052 Zarco-Tejada, P.J., Miller, J.R., Morales, A., Berjón, A., Agüera, J., 2004. Hyperspectral indices and model
 1053 simulation for chlorophyll estimation in open-canopy tree crops. *Remote Sens. Environ.* 90, 463–476.

- 1054 doi:10.1016/j.rse.2004.01.017
- 1055 Zartaloudis, Z., Savvidis, G., Savvidis, K., Iatrou, M., Glavenas, D., 2015. Early and timely detection of
1056 Verticillium dahliae in olive growing using remote sensing, in: El Aceite de Oliva. Actas Simposio
1057 Expoliva 2015. Jaén (España), p. 7.
- 1058 Zheng, G., Moskal, L.M., 2009. Retrieving Leaf Area Index (LAI) Using Remote Sensing: Theories, Methods
1059 and Sensors. *Sensors* 9, 2719–2745. doi:10.3390/s90402719

1060 **Figure captions**

1061 **Fig. 11.** Study areas localization based on high spatial resolution WorldView-3 satellite images presented in true
1062 color band combination (RGB 5-3-2) (Acquisition date: A, 24 June 2016; B, 2 July 2016).

1063 **Fig. 12.** A synthetic flow-chart showing the implemented semi-automated processing workflow to derive
1064 vegetation indices (VIs) at tree crown details from WorldView-3 (WW3) imagery.

1065 **Fig. 13.** Geographic object-based image analysis (GEOBIA) sequenced feature model process nodes for the
1066 extraction of olive tree crowns. (I): a subset of the corrected WorldView-3 (WV-3) satellite imagery, presented
1067 in a false infrared color band combination (RGB 7-5-3); (II): raster pixel processor; (III): raster object creator;
1068 (IV-V): raster object operators; (VI): raster to vector conversion; (VII): vector object operator; (VIII): vector
1069 object processor; (IX): extracted olive tree crown boundaries [yellow line] overlapped on the input image.

1070 **Fig. 14.** WV-3 scene subset of the two olive orchards (acquisition date[A] 24 June 2016; [B] 2 July 2016)) showed
1071 with vegetation enhancement color band combination (RGB 7-6-5). In each study area, in red, are highlighted
1072 the four plots defined for accuracy assessment of geographic object-based image classification (GEOBIA) and
1073 for statistical analyses of spectral behavior of olive trees [Top left, study area A. Top right, study area B. Down
1074 left and down right, image detail of plot A₂ and B₁, respectively, with superimposed (in yellow) the polygonal
1075 boundaries of tree crowns obtained through GEOBIA classification and extraction].

1076 **Fig. 15.** Relationship between number of reference trees and number of correctly detected trees in the eight
1077 investigation plots.

1078 **Fig. 16.** Vegetation indices (VIs) maps of study area A

1079 **Fig. 17.** Vegetation indices (VIs) maps of study area B

1080 **Fig. 18.** Maps of Normalized Difference Red Edge (NDRE) and Modified Chlorophyll Absorption Ratio Index
1081 Improved (MCARI2) Vegetation indices (VIs) at tree crown detail of study area A.

1082 **Fig. 19.** Maps of Normalized Difference Red Edge (NDRE) and Modified Chlorophyll Absorption Ratio Index
1083 Improved (MCARI2) Vegetation indices (VIs) at tree crown detail of study area B

1084 **Fig. 20.** Box-and-whisker plots of single WV-3 bands reflectance values variability in each study area plot (A1-
1085 A4 and B1-B4).

1086 **Table captions**

1087 **Table 11** - WorldView-3 sensor wavelength bands [nm] and relative ground sample distance [GSD] details
1088 (centered wavelength in brackets).

1089 **Table 12** - Formulation of the five vegetation indices (VIs) used in the present research.

1090 **Table 13** - Accuracy assessment of classified study area images derived from GEOBIA and olive sample trees
1091 cue metrics [(± n): ± st.dev].

1092 **Table 14** - Results and accuracy indicators of the olive tree crown extraction (TP, true positive; FP, false
1093 positive; FN, false negative; *r*, recall; *p*: precision).

1094 **Table 15** - Univariate statistics of Vegetation indices (VIs) map values, for each plot, inside A and B study areas

1095 **Table 16** - Pairwise correlations among the eight bands of WorldView-3 (WV-3) imagery, computed from the
1096 reference sample trees of A study area. Correlation values are given in the lower triangle of the matrix, and the
1097 two-tailed probabilities are given in the upper (Correlations >0.75 in bold letters, ns: no significance; **p*<0.01,
1098 ***p*<0.05).

1099 **Table 17** - Pairwise correlations among the eight bands of WorldView-3 (WV-3) imagery, computed from the
1100 reference sample trees of B study area. Correlation values are given in the lower triangle of the matrix, and the
1101 two-tailed probabilities are given in the upper (Correlations >0.75 in bold letters, ns: no significance; **p*<0.01,
1102 ***p*<0.05).

1103 **Table 18** - Summary of normality, homoscedasticity tests and ANOVA statistics result of all grouped band
1104 reflectance value, among all A plots. Summary of post-hoc test for significant band comparison [ns: no
1105 significance; different letters indicate the different plots where single band reflectance values significantly differ
1106 (*p* < 0.05)].

1107 **Table 19**. Summary of normality, homoscedasticity tests and ANOVA statistics result of all grouped band
1108 reflectance value, among all B plots. Summary of post-hoc test for significant band comparison [ns: no
1109 significance; different letters indicate the different plots where single band reflectance values significantly differ
1110 (*p* < 0.05)].